

Citation for the published version:

Kouadria, S., Berkouk, E. M., Messlem, Y., & Denai, M. (2018). Improved control strategy of DFIG-based wind turbines using direct torque and direct power control techniques. *Journal of Renewable and Sustainable Energy*, 10(4), [043306].
<https://doi.org/10.1063/1.5023739>

Document Version: Accepted Version

Link to the final published version available at the publisher:

<https://doi.org/10.1063/1.5023739>

General rights

Copyright© and Moral Rights for the publications made accessible on this site are retained by the individual authors and/or other copyright owners.

Please check the manuscript for details of any other licences that may have been applied and it is a condition of accessing publications that users recognise and abide by the legal requirements associated with these rights. You may not engage in further distribution of the material for any profitmaking activities or any commercial gain. You may freely distribute both the url (<http://uhra.herts.ac.uk/>) and the content of this paper for research or private study, educational, or not-for-profit purposes without prior permission or charge.

Take down policy

If you believe that this document breaches copyright please contact us providing details, any such items will be temporarily removed from the repository pending investigation.

Enquiries

Please contact University of Hertfordshire Research & Scholarly Communications for any enquiries at rsc@herts.ac.uk

Improved Control Strategy of DFIG-Based Wind Turbines Using Direct Torque and Direct Power Control Techniques

Selman Kouadria ^{1,2*}, El Madjid Berkouk ¹, Youcef Messlem ² and Mouloud Denai ³

¹LCP, Laboratoire de Commande des Processus, Ecole Nationale Polytechnique Algiers, Algeria

²LGEP, Laboratoire de Génie électrique et des plasmas, Université Ibn Khaldoun, Tiaret, Algeria

³School of Engineering & Technology, University of Hertfordshire, Hatfield AL10 9AB, UK

Corresponding author. Tel.:00213555118691; Fax: 0021346211796

E-mail : kouadria.selman@gmail.com

Abstract: The paper presents different control strategies for a variable-speed wind energy conversion system (WECS), based on the doubly-fed induction generator (DFIG). Direct Torque Control with Space-Vector Modulation (DTC-SVM) is used on the rotor side converter (RSC). This control method is known to reduce the fluctuations of the torque and flux at low speeds in contrast to the classical DTC, where the frequency of switching is uncontrollable. The reference for torque is obtained from the MPPT technique of the wind turbine. For the grid-side converter (GSC), a Fuzzy Direct Power Control (F-DPC) is proposed for the control of the instantaneous active and reactive power. Simulations results of the WECS are presented to compare the performance of the proposed and the classical control approaches.

1. Introduction

In Recent years and owing to the rapid decline of fossil fuels and increase in global warming, the attention is diverted towards the adoption of renewable energy sources such as wind, solar, biomass, geothermal and small hydroelectric. Wind is an abundant source of energy worldwide and is playing a vital role for electrical power generation compared to other renewable sources ^{1,2}. Because of the randomness of wind speed in different areas, a flexible electric generation system is required to maintain constant frequency voltage and stable power³.

Doubly-fed induction generators (DFIGs) are currently the dominant technology in modern wind turbines systems due to their variable speed operation, four-quadrant active and reactive power capability, low converter cost, and reduced power losses compared to other machine configurations such as fixed-speed induction generators or fully fed synchronous generators with fully sized converters⁴.

Field oriented control still the most commonly used control for DFIG system by using the classic Proportional Integral (PI) regulators^{5,6}. However, this method is more complex and difficult to maintain desired performances because it requires many parameters of the motor⁷.

Nowadays, direct control techniques for AC machines have found many interests due to their simplicity and high dynamic performances. Direct torque control (DTC) was first introduced by I. Takahashi in 1985⁸. the DTC directly controls the developed torque by the machine with the use of torque and flux information and selects the best voltage vector using a switching table. In 1988, the direct self-control (DSC) was developed in Germany by M. Depenprock⁹. After that, direct power control (DPC) was developed and presented in 1998 by T. Noguchi¹⁰; it's based on the same control principles as the DTC technique, the unique difference is the

directly controlled variables. In the case of the DTC, the electromagnetic torque and the rotor flux are directly controlled while in the DPC, the stator active and reactive powers are controlled¹¹.

Conventional direct control techniques of induction motors utilize hysteresis controller to compensate their errors. Due to the use of hysteresis controllers, conventional direct controllers suffers from high ripples and also switching frequency is variable. To overcome these disadvantages many improvements have introduced to Direct Control techniques such as Direct Control with Space Vector Modulation (DC-SVM). In addition, employment of intelligent control strategies has been swept all areas and applied in different industries, among them artificial neural network, the fuzzy logic control (FLC) and sliding mode control (SMC) have been used successfully for DFIG control¹².

The aim of this paper is to design and compare two different control methods for the rotor side power converter (RSC) and grid side power converter (GSC). For the RSC, direct torque control strategy (DTC), constructed around two hysteresis controllers, provides flux and torque regulation. For the GSC, direct power control (DPC) based on two hysteresis controllers regulates the instantaneous real and reactive power injected into the grid. These two classical control strategies are compared with DTC based on Space Vector Modulation (DTC-SVM) and fuzzy DPC (F-DPC) respectively.

The rest of the paper is organized as follows: Section 2 and 3 describe the model of wind turbine and the description of the MPPT algorithm. Section 4 presents the model of the DFIG. The design methodology of the classical DTC and DTC-SVM for the DFIG is presented in Section 5. Section 6 overviews the conventional DPC and presents the Fuzzy-DPC for the GSC. The simulation results are presented and discussed in Section 7. Finally, conclusions of the paper are presented in Section 8.

2. Modeling and control scheme of the DFIG based WECS

The WECS used in this work is depicted in Fig. 1. It consists of a wind turbine, a gearbox, a DFIG and two back-to-back two-level converters. The WECS control system consists of two main blocks: the RSC control and the GSC control. The objective of the RSC control is to decouple the active and reactive powers of the stator. In this paper, DTC-SVM is used to control the RSC. In DTC, it is possible to control machine flux and electromagnetic torque by the selection of the optimum inverter switching modes. The GSC controller, based on DPC, regulates the DC voltage and controls the power flow from the rotor of the DFIG to the grid^{13,14}.

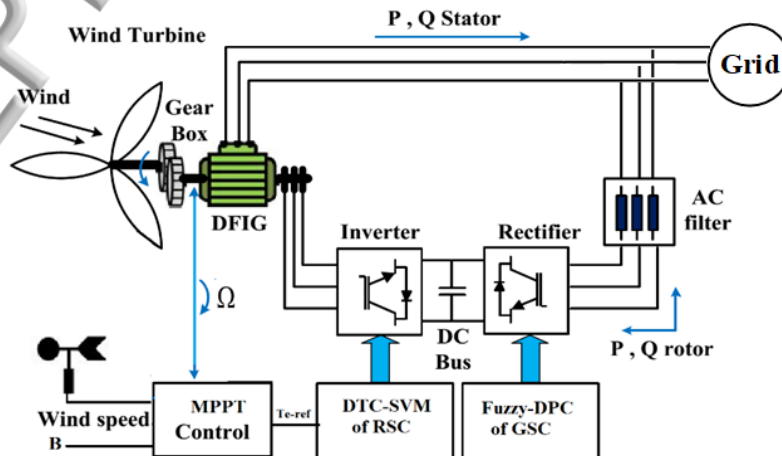


Fig. 1. Wind Energy Conversion System configuration

2.1 Modeling of the wind turbine

According to the aerodynamic characteristics of wind turbine, the output mechanical power is given by^{15,16}.

$$P_w = \frac{1}{2} \rho \pi R^2 v_t^3 C_p(\lambda, \beta) \quad (1)$$

Where ρ is the air density (kg/m^3), R is the turbine radius (m), v_t is the wind velocity (m/s) and C_p is the power coefficient defined as the ratio of the turbine power to the power of wind stream. This definition shows that power coefficient is a function of the tip speed ratio (λ) and the blade pitch angle (β), being tip speed ratio the ratio of the speed at the tip of the blade to wind velocity¹⁷.

$$\lambda = \frac{\omega_t R}{v_t} \quad (2)$$

In general, the aerodynamic torque of the wind turbine can be expressed as¹⁸

$$T_w = \frac{1}{2} \frac{\rho \pi R^3 v_t^2 C_p(\lambda, \beta)}{\lambda} \quad (3)$$

The performance coefficient is different for each turbine and is related to the tip speed ratio and pitch angle. A generic equation is used to model $C_p(\beta, \lambda)$. This equation, based on the modeling turbine characteristics, is¹⁸⁻²¹:

$$C_p(\lambda, \beta) = C_1 \left(C_2 \frac{1}{\lambda^4} - C_3 \beta - C_4 \right) e^{\frac{C_5}{\lambda}} + C_6 \lambda \quad (4)$$

With

$$\frac{1}{\lambda_t} = \frac{1}{\lambda + 0.08 \beta} - \frac{0.035}{\beta^3 + 1} \quad (5)$$

Table I gives the parameters C1 to C6.

Table I: Parameters of the performance coefficient

C_1	C_2	C_3	C_4	C_5	C_6
0.5176	116.0	0.4	5.0	21.0	0.0068

2.2 Maximum Power Point Tracking (MPPT) technique

Maximum power point tracking (MPPT) strategies play an important role in wind power conversion systems (WECS) because they maximize the power extracted from the wind, and therefore optimize the conversion efficiency. Two strategies are commonly used²²⁻²⁴, based on whether speed control is used or not. In this paper, the MPPT with speed control is used as it permits to adjust the wind turbine speed to the desired value which corresponds to the maximum power extraction. The power extracted from the wind is maximized when C_p is optimal. This optimal value of C_p occurs at a defined value of the tip speed ratio λ . For each wind speed, there is an optimum rotor speed where maximum power is extracted from the wind. Therefore, if wind speed is assumed to be constant, the value of C_p depends only on the rotor speed of the wind turbine. The variability of the output power from the wind generator implies that, without special interface measures, the turbine will often operate away from its maximum power point. The associated losses can be avoided by the use of an

MPPT controller which ensures that there is always maximum energy transfer from the wind turbine to the grid²⁵⁻²⁷.

The simplified representation of wind turbine model with speed control is given in Fig.2.

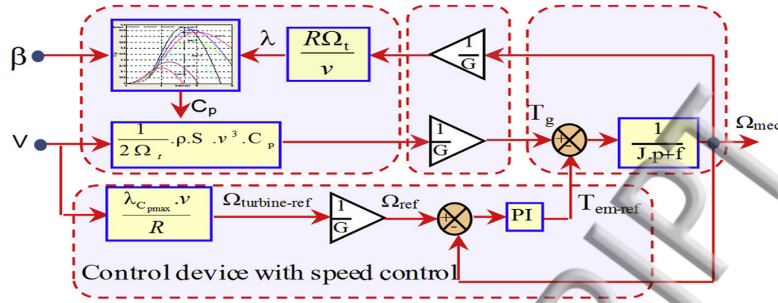


Fig. 2. Diagram block of the MPPT extracted with speed control

The maximum value of CP (CP max = 0.48) is achieved for $\beta = 0$ and for $\lambda = 8.12$. To achieve this step, the value of the electromagnetic torque reference is set at the maximum value given by^{2,28,29}:

$$T_{em-ref} = \frac{1}{2} \frac{\rho \pi R_t^5 C_{pmax}}{\lambda_{opt}^3 G^3} \Omega_{mec}^2 \quad (6)$$

Fig.3 shows the $C_p(\beta, \lambda)$ characteristics for different values of the pitch angle β ¹⁹.

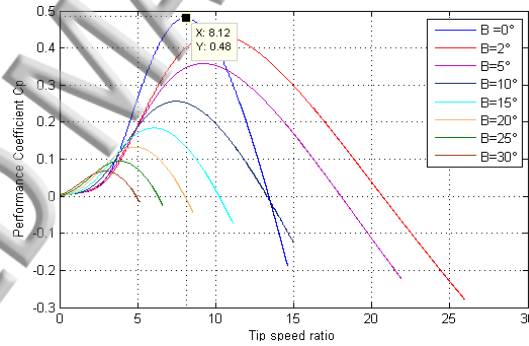


Fig 3: The typical performance coefficient curve

2.3 Modeling of the DFIG

A commonly used model for the DFIG is the Park model^{30,31}. Where the stator and rotor voltages are given as follows:

$$\begin{cases} V_{ds} = R_s I_{ds} + \frac{d\phi_{ds}}{dt} - \omega_s \phi_{qs} \\ V_{qs} = R_s I_{qs} + \frac{d\phi_{qs}}{dt} + \omega_s \phi_{ds} \\ V_{dr} = R_r I_{dr} + \frac{d\phi_{dr}}{dt} - (\omega_s - \omega_r) \phi_{qr} \\ V_{qr} = R_r I_{qr} + \frac{d\phi_{qr}}{dt} + (\omega_s - \omega_r) \phi_{dr} \end{cases} \quad (7)$$

The stator and rotor flux are given as:

$$\begin{cases} \varphi_{ds} = L_s I_{ds} + L_m I_{dr} \\ \varphi_{qs} = L_s I_{qs} + L_m I_{qr} \\ \varphi_{dr} = L_r I_{dr} + L_m I_{ds} \\ \varphi_{qr} = L_r I_{qr} + L_m I_{qs} \end{cases} \quad (8)$$

3. Direct Torque Control of RSC

This section presents the synthesis of two DTC control strategies for the RSC, based on two-level inverter topology, to improve the energy efficiency and performance characteristics of the variable speed wind turbine driven by the DFIG. The two DTC control strategies considered are the classical/conventional DTC and a DTC based on SVPWM control with fixed frequency defined by a parallel control structure³².

DTC was introduced by Takahashi (1984) in Japan and then in Germany by Depenbrock (1985)^{33–38} and has proved to be a powerful method for the control of induction machines. As compared to stator flux oriented control or field oriented control (FOC), DTC implementation minimizes the use of machine parameters^{32,9,39–42} while conserving the merits of fast transient response characteristics, it provides a systematic solution to improve operating characteristics of the machine and voltage inverter source⁴³. DTC method is based mainly on instantaneous space vector theory.

The application of DTC to the DFIG has been discussed in^{13,37,44–47,47–50}. The basic principle consists of selecting the inverter switching states to control directly the rotor flux linkage magnitude, φ_r , and the generator torque, T_e ⁴⁷. The selection of the appropriate voltage vectors uses a pre-defined switching table and is based on hysteresis control of the estimated rotor flux linkage and the torque. The rotor flux and torque are controlled directly and independently. The torque hysteresis comparator is a three-valued comparator. Whereas the flux hysteresis comparator is a two-valued comparator^{29,37,44}. Consequently, the number of space voltage vectors and switching frequency directly influence the performance of DTC. For a fixed switching strategy, the machine operation, in terms of torque, switching frequency, and torque response are quite different at low and high speed^{29,51,52}.

The voltage vector V_r is delivered by a three-phase voltage source inverter whose switch states are supposed ideal. It is represented theoretically by three (03) Boolean control variables S_j ($j = a, b, c$) such that when $S_j = 1$, the high switch is closed and the low switch is open and when $S_j = 0$, the high switch is open and the low switch is closed.

Consequently, the voltage vector V_r can be written in the following form^{53,51}:

$$V_r = \sqrt{\frac{2}{3}} U_{dc} [S_a + S_b e^{j\frac{2\pi}{3}} + S_c e^{j\frac{4\pi}{3}}] \quad (9)$$

3.1 Estimation of the rotor flux linkage

$$\hat{\varphi}_r = \int_0^t (V_r - R_r i_r) dt \quad (10)$$

The magnitude of the rotor flux is estimated from its components along the α and β axes^{53,29,37,44–49,51}.

$$\begin{cases} \hat{\varphi}_{r\alpha}(t) = \int_0^t (V_{r\alpha} - R_{r\alpha} i_{r\alpha}) dt \\ \hat{\varphi}_{r\beta}(t) = \int_0^t (V_{r\beta} - R_{r\beta} i_{r\beta}) dt \end{cases} \quad (11)$$

The amplitude of the rotor flux vector can be expressed by:

$$\varphi_r = \sqrt{\varphi_{r\alpha}^2 + \varphi_{r\beta}^2} \quad (12)$$

The angle α of the rotor flux φ_r is determined by:

$$\alpha_r = \tan^{-1} \left(\frac{\varphi_{r\beta}}{\varphi_{r\alpha}} \right) \quad (13)$$

3.2 Estimation of the electromagnetic torque

The electromagnetic torque can be estimated starting from the estimated value of the flux $\varphi_{r\alpha}$ and $\varphi_{r\beta}$ and the calculated values of the current $i_{r\alpha}$ and $i_{r\beta}$ ^{53,29,37,44-49,51}.

$$T_e = p(\varphi_{r\alpha} i_{r\beta} - \varphi_{r\beta} i_{r\alpha}) \quad (14)$$

Select the sector where the rotor flux vector belongs is essential. φ_r is controlled by a two-level hysteresis regulator as shown in Fig. 4, where the flux amplitude must be increased ($K=0$) and ($K=1$) to decrease it.

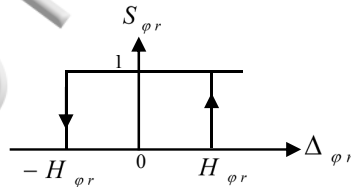


Fig. 4 Two-level hysteresis regulator

T_{em} is controlled by a 3-level hysteresis regulator as shown in Fig. 5, where the states are '1' (increase) and '-1' (decrease) and '0' (constant).

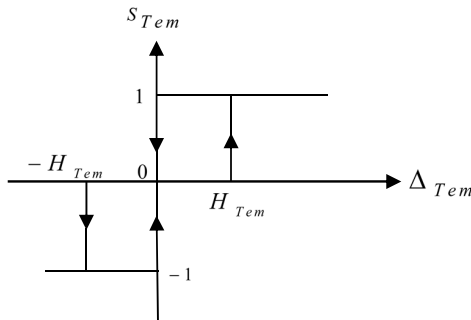


Figure 5: Three level hysteresis regulator

According to the combination of the switching modes of the Voltage Source Inverter VSI , the voltage vectors is applied to the rotor and this voltage will cause the rotor flux to change⁵². The tangential component of the rotor voltage vector will increase or decrease the torque angle, while the radial component will increase or decrease the rotor flux magnitude as depicted in, Fig. 6.

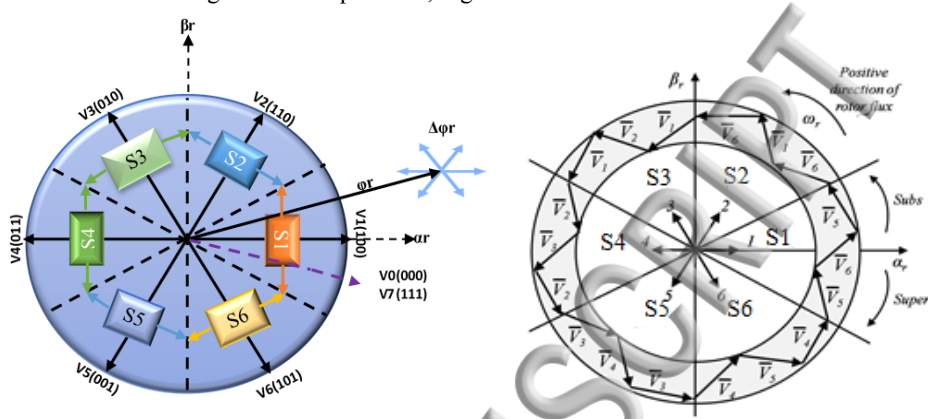


Fig. 6: Trajectory representation of rotor flux space vector with different voltage vectors

The DFIG stator winding is directly connected to the grid, which means that stator flux vector is practically constant both in magnitude and speed. As the rotor and stator fluxes are referred to a rotor reference frame, both fluxes are rotating at the slip speed on the rotor reference frame. The position of the rotor flux is divided into six sectors. Rotor flux is then controlled by means of one of eight different voltage vectors. There are six active voltage vectors $V_1 - V_6$. Each vector lies in the center of a sector of 60° width denoted S_1 to S_6 according to the voltage vector it contains, and two zero voltage vectors $V_0 - V_7$ at the origin the sector and vector placement is shown in Fig. 6^{53,29,44,46,51}.

3.3 Switching Table:

The following table II presents selection of appropriate vector applied to the rotor side converter. This table permit to control the rotor flux and the torque^{13,29,44-46,51}

Table II: selection of appropriate vector applied to the rotor side converter

		Sector (N)	1	2	3	4	5	6
$S_{\phi_r} = 1$	$S_{cem} = 1$		V_2	V_3	V_4	V_5	V_6	V_1
	$S_{cem} = 0$		V_7	V_0	V_7	V_0	V_7	V_0
	$S_{Scem} = -1$		V_6	V_1	V_2	V_3	V_4	V_5
$S_{\phi_r} = 0$	$S_{cem} = 1$		V_3	V_4	V_5	V_6	V_1	V_2
	$S_{cem} = 0$		V_0	V_7	V_0	V_7	V_0	V_7
	$S_{cem} = -1$		V_5	V_6	V_1	V_2	V_3	V_4

Where the voltage vectors are defined as:

$$V_0 = [000]; V_1 = [100]; V_2 = [110]; V_3 = [010]; V_4 = [011]; V_5 = [001]; V_6 = [101]; V_7 = [111]$$

3.4 Implementation of the classical DTC

A schematic diagram of the DTC applied to the DFIG is shown in Fig. 7. There are two loops for the control of the rotor flux and torque magnitudes. The reference values for the flux rotor and torque are compared with the actual values, and the resulting error values are fed into the two-level and three-level hysteresis blocks respectively. The outputs of the rotor flux error and torque error hysteresis blocks, together with the position of the rotor flux are used as inputs of the switching Table II. The position of the rotor flux is divided into six sectors. According to Fig. 7, the rotor flux and torque errors tend to be restricted within their respective hysteresis bands. It can be proved that the flux hysteresis band affects the rotor-current distortion in terms of low order harmonics and the torque hysteresis band affects the switching frequency⁵⁴.

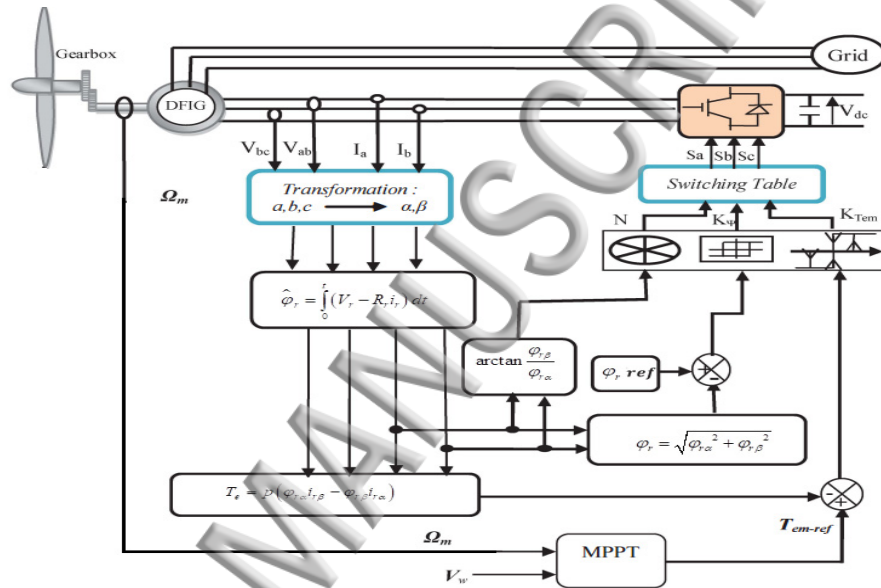


Fig. 7: Structure of the direct torque control applied to a DFIG

3.5 DTC based on Space Vector Modulation

The classical DTC does not require any mechanical sensor or current regulator and coordinate transformation is not present, thus reducing the complexity of its implementation⁵⁵. DTC has proved as an effective control strategy in various industrial applications⁵⁶. However, the performance of DTC is limited due to the presence of hysteresis control characterized by high torque and flux ripples, slow transient response to step changes during start up and a variable switching frequency^{32,41,57,58}.

Generally, there are two methods to reduce the torque and flux ripples in the DTC-controlled drives. The first is to use a multilevel inverter or multi cell inverter^{42,56,59-61}, which provides a more precise control of the torque and flux. However, the cost and complexity will be increased because more power switches are used; they are mainly used for high voltage applications. The other method uses space vector modulation (SVM). In the DTC-SVM, the torque ripple and flux ripple can be reduced with fixed frequency^{52,62-64}. In this work, the proposed DTC is based on space-vector pulse width modulation (SVPWM).

SVPWM is an advanced PWM technique now widely used in industrial variable frequency drives application. SVM provides a better fundamental output voltage, better harmonic performance, and is easy to implement^{65,66}.

Compared with sinusoidal pulse width modulation (SPWM), SVM is more suitable for real-time implementation since the obtainable DC voltage utilization ratio can be considerably increased⁶⁷⁻⁷⁰.

The basic concept of DTC with Space Vector Modulation (DTC-SVM)^{32,52,71} for the control of a DFIG is illustrated in Fig. 8. The combination of a PI controller with SVM ensures a reduction in the harmonic level of the rotor currents, allows the use of a fixed switching frequency and reduce ripples in the torque and flux response^{32,52,72-74}.

In the structure of DTC-SVM, the two inner control loops with PI controllers regulate the magnitude of the rotor flux vector and the electromagnetic torque of the DFIG. The magnitude of the rotor flux vector ϕ_r and the value of the electromagnetic torque T_e are compared with their reference values. Both error signals are sent to two PI controllers. The output control signals from PI controllers determine the reference values v_{rx}^* and v_{ry}^* of the stator voltage vector components of RSC^{32,52,57,63,75-82}.

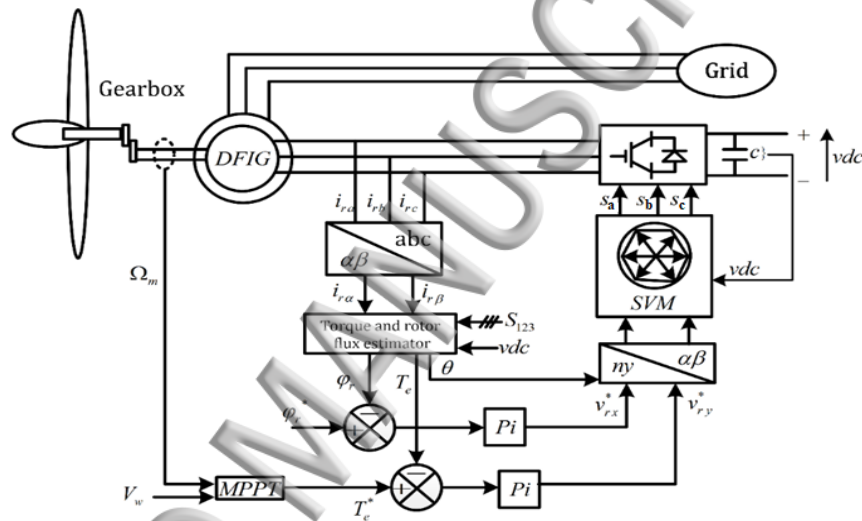


Fig. 8: Control diagram of DTC-SVM for Rotor Side Converter

4. Direct power control of GSC

In a DFIG-based wind turbine, the main objective of the grid side converter GSC is to maintain a constant DC link voltage and to control the flow of the power delivered to the grid. In this work, Direct Power Control (DPC) is used to achieve these control objectives.

DPC is based on the same control principles as DTC. The only difference is in the directly controlled variables. In DTC, the electromagnetic torque and the rotor flux are the directly controlled variables, while in DPC, the active and reactive powers are directly controlled by selecting the optimum switching state of the converter⁸³⁻⁸⁷.

DPC based on the instantaneous active and reactive power control loops was developed for controlling PWM rectifiers connected to the network⁸⁸. In this technique, there are no internal current control loops and no PWM modulator block. The PWM voltage source converters switching states is determined by a switching table based on the instantaneous errors between the actual and estimated values of the active and reactive powers. Fig.9 shows the configuration of the direct instantaneous active and reactive power control for a three-phase PWM rectifier^{89,90}.

The instantaneous active (P) and reactive (Q) powers are estimated using voltage and current measurements, and compared to their references P^* and Q^* respectively. Reference P^* is provided from the PI regulator of the DC voltage controller block whereas reference Q^* is set to zero to achieve a unity power factor. The instantaneous errors between the actual and estimated powers are controlled directly with hysteresis controllers and a lookup table like the one used in DTC ⁶³.

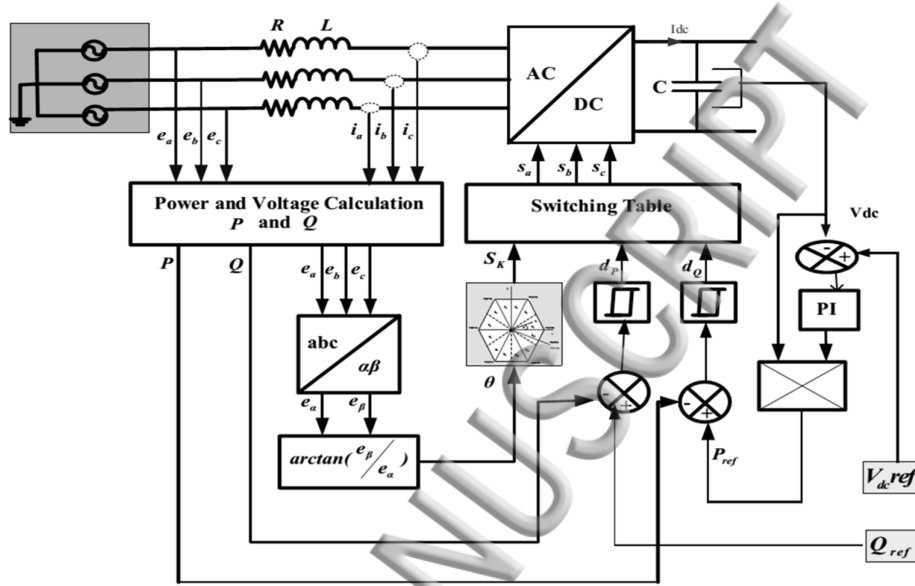


Fig. 9: Bloc diagram of DPC for Grid Side Converter

The error signals S_p, S_q , and voltage phase angle θ_n are fed to the switching table (Table III) which stores the states S_a, S_b , and S_c , of the converter. The optimal switching states are selected so that the power errors are kept within the hysteresis bands. For this purpose, the stationary coordinates are divided into 12 sectors, as shown in Fig. 10, and the sectors can be numerically expressed as:

$$\theta = \tan^{-1} \left(\frac{v_\beta}{v_\alpha} \right) \quad (20)$$

$$(n-2)\frac{\pi}{6} \leq \theta_n < (n-1)\frac{\pi}{6} \text{ where } n=1,2,3,\dots,12 \quad (21)$$

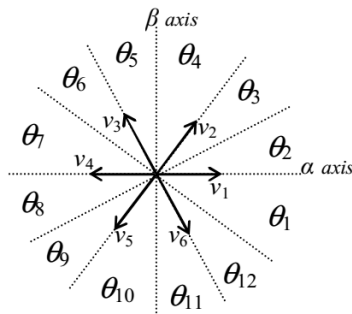


Fig. 10: Sectors and voltage vectors of VSI

The instantaneous active and reactive power are given by⁹¹.

$$\begin{aligned}
 p &= v_a i_a + v_b i_b + v_c i_c \\
 q &= \frac{1}{\sqrt{3}} [(v_b - v_c) i_a + (v_c - v_a) i_b + (v_a - v_b) i_c]
 \end{aligned}
 \tag{22}$$

Table III: Switching table of GSC

d_p	d_q	θ_1	θ_2	θ_3	θ_4	θ_5	θ_6	θ_7	θ_8	θ_9	θ_{10}	θ_{11}	θ_{12}
1	0	v_5	v_6	v_6	v_1	v_1	v_2	v_2	v_3	v_3	v_4	v_4	v_5
	1	v_3	v_4	v_4	v_5	v_5	v_6	v_6	v_1	v_1	v_2	v_2	v_3
0	0	v_6	v_1	v_1	v_2	v_2	v_3	v_3	v_4	v_4	v_5	v_5	v_6
	1	v_1	v_2	v_2	v_3	v_3	v_4	v_4	v_5	v_5	v_6	v_6	v_1

4.1. Hysteresis Controller

The main idea behind DPC method is to maintain the instantaneous active and reactive power within a desired band. DPC consists of two hysteresis comparators whose inputs are the errors between the reference and estimated values of the active and reactive power respectively⁹²:

$$\begin{cases}
 \Delta p = p_{ref} - p \\
 \Delta q = q_{ref} - q
 \end{cases}
 \tag{23}$$

The hysteresis comparators provide two logic outputs d_p and d_q . The state “1” corresponds to an increase of the controlled variable (p and q) while “0” corresponds to a decrease.

$$\begin{cases}
 \text{if } \Delta p \geq h_p \Rightarrow d_p = 1 \\
 \text{if } \Delta p < -h_p \Rightarrow d_p = 0 \\
 \text{if } \Delta q \geq h_q \Rightarrow d_q = 1 \\
 \text{if } \Delta q < -h_q \Rightarrow d_q = 0
 \end{cases}
 \tag{24}$$

Where h_p and h_q denote the hysteresis bands.

4.2. Fuzzy Direct power Control:

A block diagram of the proposed fuzzy direct power control (Fuzzy-DPC) technique is shown in Fig. 11.

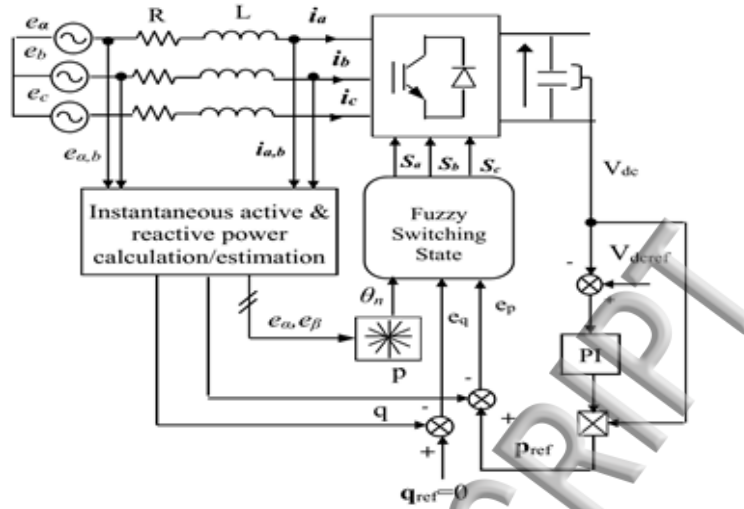


Fig. 11: The proposed structure of fuzzy direct power control

In this control scheme, the hysteresis controllers are replaced by fuzzy logic controllers (FLC) however, it uses the same concept as DPC for the selection of the switching vector. The inputs to the FLC are the errors of real and reactive power (e_p , e_q) and their variations (de_p , de_q) and the output of the FLC is the actual voltage vector applied to the GSC^{93,6}.

$$\begin{cases} e_p = p_{ref}(k) - p(k) \\ de_p = e_p(k) - e_p(k-1) \\ e_q = q_{ref}(k) - q(k) \\ de_q = e_q(k) - e_q(k-1) \end{cases} \quad (25)$$

The inference method used is based on Mamdani min-max rule. The membership functions of the input and the output variables are shown in Fig. 12. With seven fuzzy sets labeled: negative big (NB), negative medium (NM), negative small (NS), zero (Z), positive small (PS), positive medium (PM) and positive big (PB). The resulting rules are presented in Table IV.

Table IV: Table FLC rule base

de \ e	PB	PM	PS	Z	NS	NM	NB
PB	PB	PB	PB	PB	PM	PS	Z
PM	PB	PB	PB	PM	PS	Z	NS
PS	PB	PB	PM	PS	Z	NS	NM
Z	PB	PM	PM	Z	NM	NM	NB
NS	PM	PS	Z	NS	NM	NB	NB
NM	PS	Z	NS	NM	NB	NB	NB
NB	Z	NS	NM	NB	NB	NB	NB

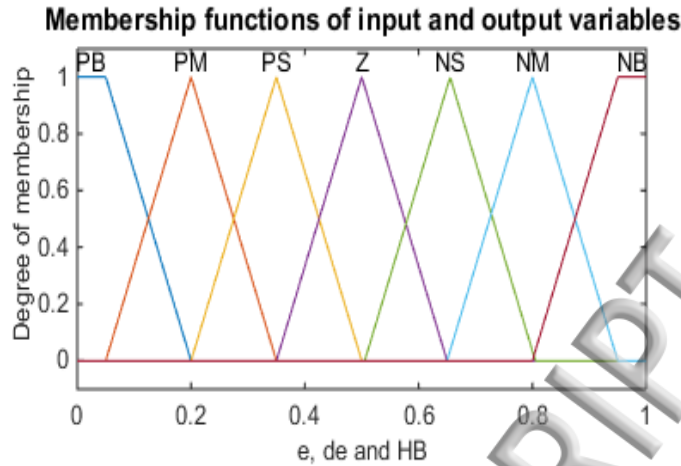


Fig. 12: Membership functions for the input and output variables of the active and reactive powers

5. Simulations results

The WECS used in these simulations is based on 10 kW wind turbine and a 7.5 kW DFIG connected to the grid and the model is implemented in Matlab /Simulink environment. The parameters values used in the models are presented in the Appendix.

The wind speed profile used in these simulations is shown in Fig. 13 (a). For the simulated wind turbine model, the maximum power coefficient $C_{p,max} = 0.48$ and the optimal tip speed ratio = 8.1 (Fig. 13 (c) and (d)).

Fig. 13 (b) shows the waveforms of optimal angular speed ω_{opt} and the measured angular rotor speed ω_m of the DFIG. The reference angular rotor speed ω_{opt} is obtained from the MPPT algorithm.

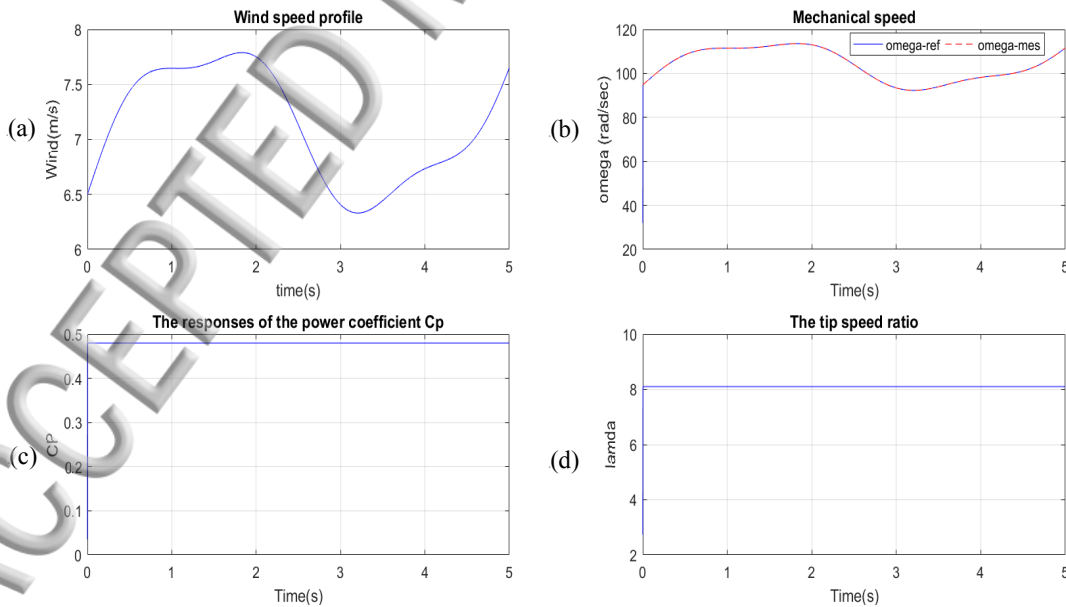


Fig. 13: Wind turbine characteristics.

(a) wind speed profile, (b) mechanical speed, (c) power coefficient (C_p), (d) tip speed (λ).

Fig. 14 presents different switching schemes present in two-level SVPWM.

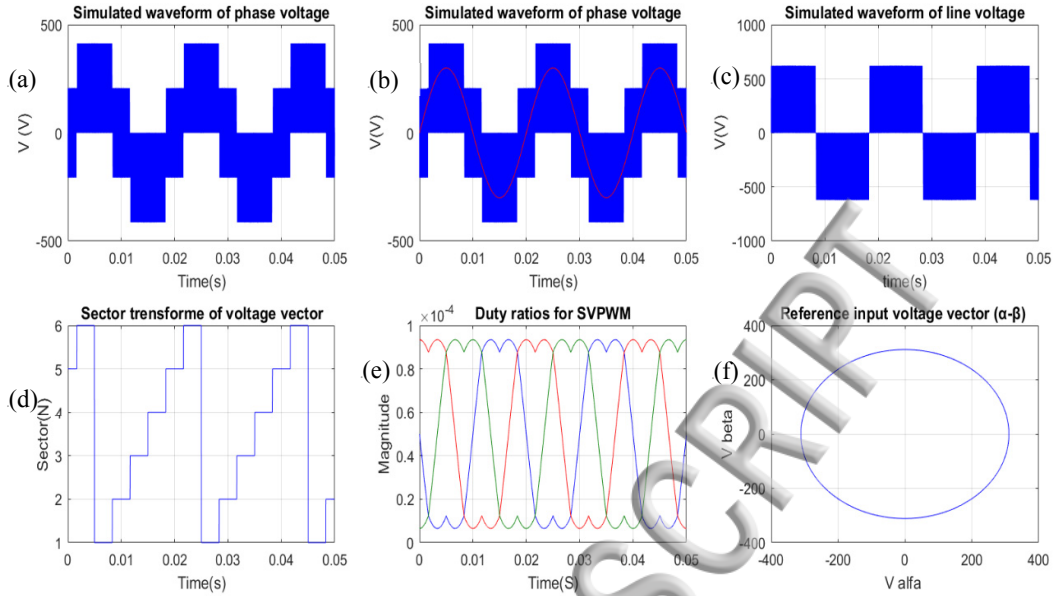


Fig. 14: Switching schemes in two level SVPWM
 (a) ,(b) Waveform of phase voltage, (c) Waveform of line voltage, (d) Sector transform of voltage vector, (e) Duty ratios for SVPWM, (f) Reference input voltage vector (α - β) .

Fig. 15 presents the results with the classical DTC. It can be noticed that the torque reacts quickly to changes in wind speed.

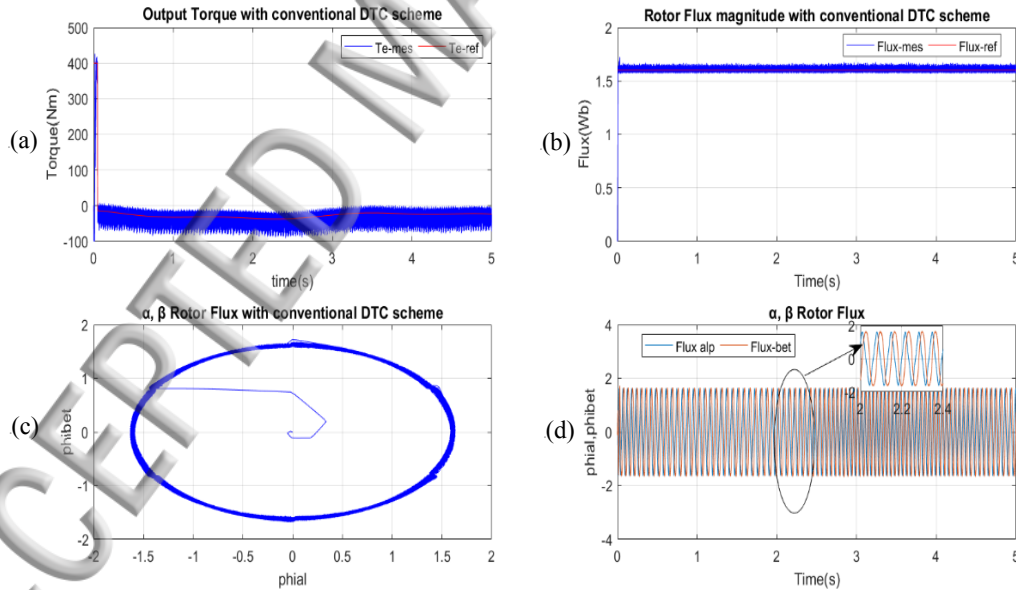


Fig. 15: Response of RSC with DTC
 (a)Output of the torque, (b) Rotor flux magnitude, (c) α - β rotor flux , (d) α - β rotor flux

The results obtained with DTC-SPWM are shown in Fig. 16. From Fig. 16(c), the trajectory of the rotor flux vector, it can be stated that the rotor flux vector rotates with a constant magnitude and with small oscillation. Overall, the DTC-SVPWM with a two-level inverter resulted in a better performance with a significant reduction in the torque and flux ripples and a rapid system response.

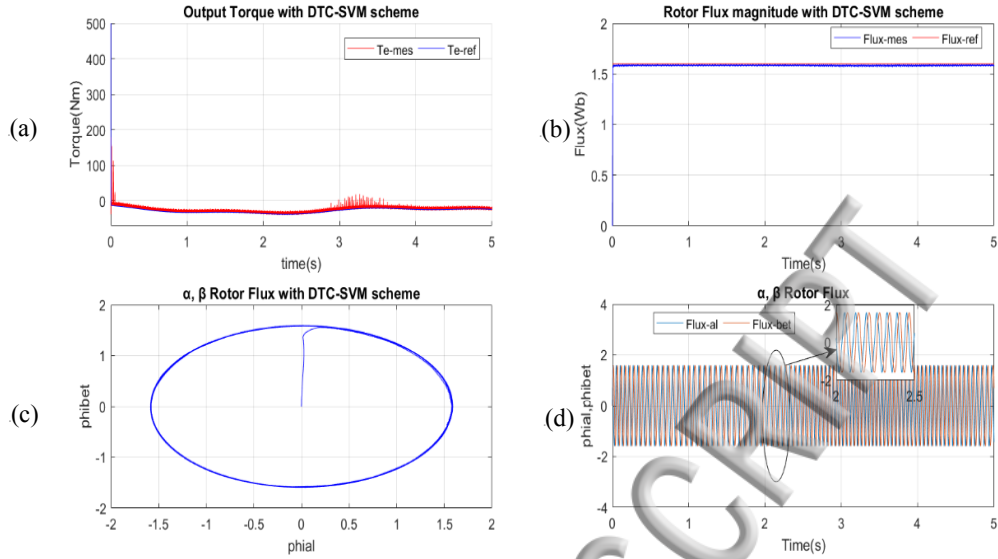


Fig. 16: Response of RSC with DTC-SVM.

(a) Output torque, (b) Rotor flux magnitude, (c) α - β rotor flux, (d) α - β rotor flux

The response of the DC-link voltage is shown in Fig. 17. The instantaneous value of DC-link voltage is kept constant across a wide range of variations of the wind speed.

Fig. 17 shows the instantaneous active p_g and reactive power q_g delivered to the AC grid when DPC is applied to the DFIG. The instantaneous reactive power q_g is set to zero to achieve a unity power factor. The instantaneous active power delivered to the AC grid varies because of the fluctuating wind speed.

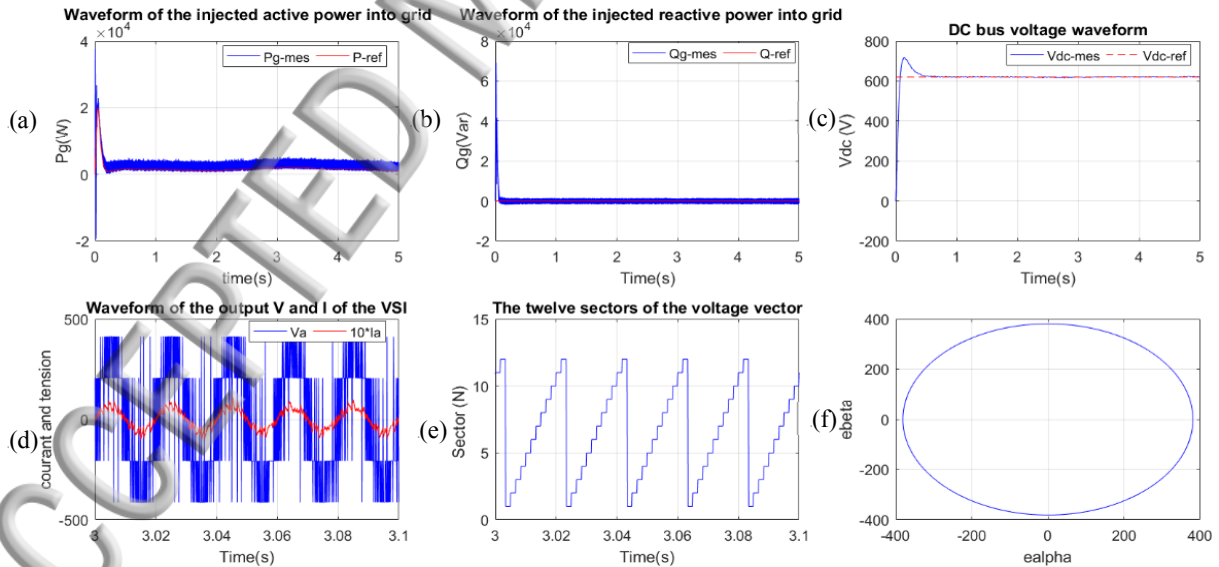


Fig. 17: Response of GSC with DPC.

(a) The injected active power into grid, (b) The injected reactive power into grid, (c) DC bus voltage (d) output V and I of the VSI (e) the twelve sectors of the voltage vector, (f) Reference input voltage vector (α - β)

The results in Fig. 18 are obtained with the proposed Fuzzy-DPC. A very good control of the DC bus voltage is achieved. It can be observed from these simulation that the control of the GSC with Fuzzy-DPC resulted in better steady and transient response and significant reduction in the instantaneous active p_g and reactive power q_g ripples.

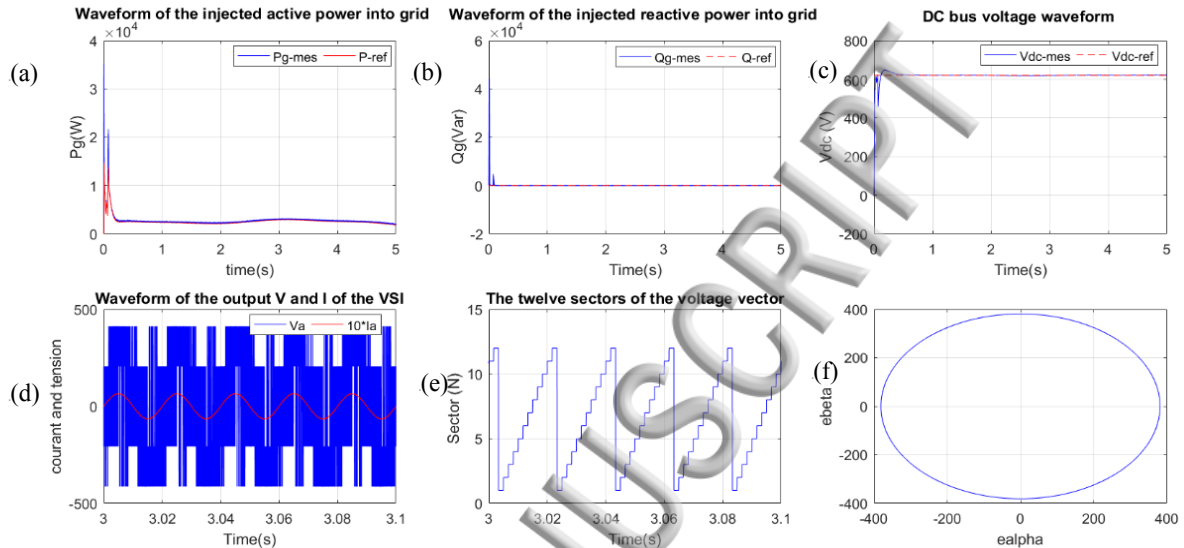


Fig. 18: Response of GSC with Fuzzy-DPC

(a) The injected active power into grid, (b) The injected reactive power into grid, (c) DC bus voltage (d) output V and I of the VSI (e) the twelve sectors of the voltage vector, (f) Reference input voltage vector (α - β)

6. Conclusion

In this paper, a control of a DFIG-driven wind turbine is investigated by testing a different control strategy in both side of DFIG: Rotor Side Converter (RSC) and Grid Side Converter (GSC). A direct torque control (DTC) and a DTC based on space vector modulation (DTC-SVM) was designed and compared for (RSC) and the simulation results showed that the conventional (C-DTC) strategy presents a fast and good dynamic torque in steady state behavior. However, due of the variable switching frequency, this strategy presents the drawback of having a high switching frequency. The latter introduce high ripples of flux and electromagnetic torque. The torque and flux ripples can be reduced significantly and low constant switching frequency is achieved with the proposed DTC-SVM strategy. Besides, for the grid side converter (GSC): a direct power control (DPC) and a fuzzy direct power control (FDPC) have been implemented and the presented results showed that the conventional DPC (C-DPC) strategy has a fast and good dynamic in steady state behavior. Nonetheless, this strategy presents high active and reactive power ripples. Therefore, these ripples can be reduced significantly and very good control of the DC bus voltage is achieved with the proposed FDPC strategy.

The simulation results for every case (DTC, DTC-SVM, DPC, Fuzzy-DPC), confirmed the high effectiveness of the proposed methods (DTC-SVM and Fuzzy-DPC).

7. Appendix

Appendix A: System Parameters

Table V: Wind turbine parameters

Nominal power (P)	10KW
Diameter (D)	3m
Number of blades	3
Gearbox (G)	5.4
Inertial (J)	0.042 Kg.m ²
Viscous coefficient (f)	0.017 N.m.s ⁻¹

Table VI: Doubly fed induction generator parameters

Nominal power (P)	7.5KW
Nominal speed (N)	1500 rpmn
Stator resistance (Rs)	0.455 Ω
Rotor resistance (Rr)	0.62 Ω
Stator inductance (Ls)	0.084 H
Rotor inductance (Lr)	0.081H
Main inductance (Lm)	0.078 H
Pairs of pole number (p)	2
Inertial (J)	0.3125 Kg.m ²
Viscous coefficient (f)	6.73.10 ⁻³ N.m.s ⁻¹

Appendix B:

B.1. Principle of SVPWM

The basic principle of Space vector PWM for a two-level voltage source inverter is that which treats sinusoidal voltage as a rotating constant amplitude vector rotating with constant frequency^{69,94,95}, and generating three consecutive switching voltage vectors in a sampling period (T_s) and approximates the reference voltage V_{ref} by the combination of different switching modes of the inverter⁹⁶.

To implement the space vector PWM, the abc reference of the voltage equations can be transformed into the stationary $\alpha\beta$ reference frame^{97,98}. There are eight switching states for the inverter at any instant of time. Out of which six switching states [(100), (110), (010), (011), (001), (101)] produce a non-zero voltage vectors (V1,V2,V3,V4,V5,V6), and the remaining two switching states [(111), (000)] produce zero voltage vectors (V0,V7)⁹⁹.

The vectors (V1 - V6) are working states that form stationary vectors in the $\alpha\beta$ frame and divide the plane into six sectors (each sector: 60 degrees)¹⁰⁰ and shape form a hexagon as depicted in Fig.19⁹⁸ and feed electric power to the load or DC link voltage is supplied to the load. The angle between any adjacent two nonzero vectors is 60 degrees¹⁰¹.

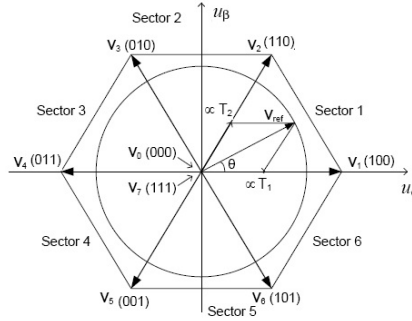


Fig. 19: Diagram of the inverter exported voltage space vector

B.2. Steps in the realization of blocks SVM

In general, the Conventional SVPWM implementation involves the following six steps:

- (a) Determination of reference voltages V_α , V_β , (b) sector identification in which the instantaneous reference space vector lies, (c) calculation of the variables X, Y and Z, (d) calculation of T_1 and T_2 for each sector, (e) generation of the modulating signals T_{aon} , T_{bon} and T_{con} , (f) pulse generation series T_a , T_b and T_c .

B.2.a. Determining v_α , v_β

Fig. 20 is the typical diagram of a three-phase voltage source inverter model^{102,103}.

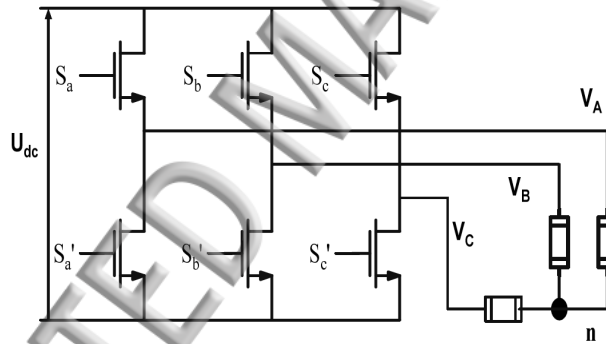


Figure 20: Typical diagram of a three-phase inverter

Space Vector Modulation (SVM) is based on the representation of the three phase measures as vectors into two dimensions (α , β) plane^{104,105}.

$$\begin{bmatrix} V_\alpha \\ V_\beta \end{bmatrix} = \frac{U_{dc}}{3} \begin{bmatrix} 2 & -1 & -1 \\ 0 & \sqrt{3} & -\sqrt{3} \end{bmatrix} \begin{bmatrix} S_a \\ S_b \\ S_c \end{bmatrix} \quad (25)$$

The V_{ref} and angle (θ) are given as in the equations (3) & (4)

$$V_{ref} = \sqrt{V_\alpha^2 + V_\beta^2} \quad (27)$$

$$\theta = \tan^{-1} \left(\frac{V_{\beta}}{V_{\alpha}} \right) \quad (29)$$

B.2.b. Identifying sectors

This step is to identify the sector in which the reference voltage space vector is present. It is necessary to know in which sector the reference output lies in order to determine the switching time and sequence. The identification of the sector where the reference vector is located is straight forward. The phase voltage corresponding to eight switching states: six non-zero vectors and two zero vectors at the origin. Depending on the reference voltages, the angle of the reference vector can be determined the sector as per the table VII¹⁰⁶.

Table VII: Sectors and their respective angle

Ni	Sector 1	Sector 2	Sector 3	Sector 4	Sector 5	Sector 6
θ	$0 \leq \theta \leq \frac{\pi}{3}$	$\frac{\pi}{3} \leq \theta \leq \frac{2\pi}{3}$	$\frac{2\pi}{3} \leq \theta \leq \pi$	$\pi \leq \theta \leq \frac{4\pi}{3}$	$\frac{4\pi}{3} \leq \theta \leq \frac{5\pi}{3}$	$\frac{5\pi}{3} \leq \theta \leq 2\pi$

B.2.c. Calculation of variables X, Y and Z

The rest of the period spent in applying the null vector. For every sector, commutation duration is calculated. The amount of times of vector application can all be related to the following variables¹⁰⁷⁻¹⁰⁹.

The three variables are given by the following equations:

$$\begin{aligned} X &= \sqrt{3} \frac{T_s}{U_{dc}} V_B \\ Y &= \frac{T_s}{2U_{dc}} (\sqrt{3}V_{\beta} + 3V_{\alpha}) \\ Z &= \frac{T_s}{2U_{dc}} (\sqrt{3}V_{\beta} - 3V_{\alpha}) \end{aligned} \quad (30)$$

T_s is the sampling time and V_{dc} is the DC voltage on one side of the inverter¹¹⁰.

B.2.d. Calculation of T_1 and T_2

The application durations of the sector boundary vectors are tabulated as follows¹⁰⁹:

In this step, the determination of the times T_1 and T_2 for each sector from the values of X, Y and Z according to the Table VIII¹¹⁰.

Table VIII: Calculation of T_1 and T_2

Sector	1	2	3	4	5	6
T_1	-Z	Y	X	Z	-Y	-X
T_2	X	Z	-Y	-X	-Z	Y

B.2.e. Determination of T_{aon} , T_{bon} and T_{con}

This step is to compute the three necessary duty cycles as:

$$\begin{aligned}
 T_{aon} &= \frac{T_s - (T_1 + T_2)}{2} \\
 T_{bon} &= T_{aon} + T_1 \\
 T_{con} &= T_{bon} + T_2
 \end{aligned}
 \tag{31}$$

B.2.f. Determination of Ta, Tb and Tc

The last step is to assign the right duty cycle (T_{xon}) to the right motor phase according to the sector¹⁰⁹. The T_{xon} signals are ordered in a certain way (Table IX)¹¹⁰.

Table IX: Calculation of Ta, Tb and Tc

Sector phase	1	2	3	4	5	6
Ta	T_{aon}	T_{bon}	T_{con}	T_{con}	T_{bon}	T_{aon}
Tb	T_{bon}	T_{aon}	T_{aon}	T_{bon}	T_{con}	T_{con}
Tc	T_{con}	T_{con}	T_{bon}	T_{aon}	T_{aon}	T_{bon}

After all the mathematical equations have been derived, then all the equations are modelled in Matlab/Simulink to generate the switching signal. Fig 21 shows the overall model of SVPWM¹⁰³.

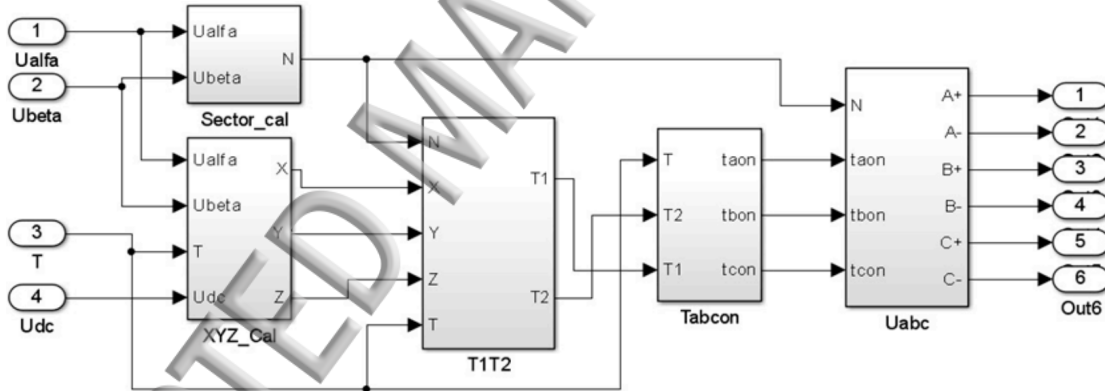


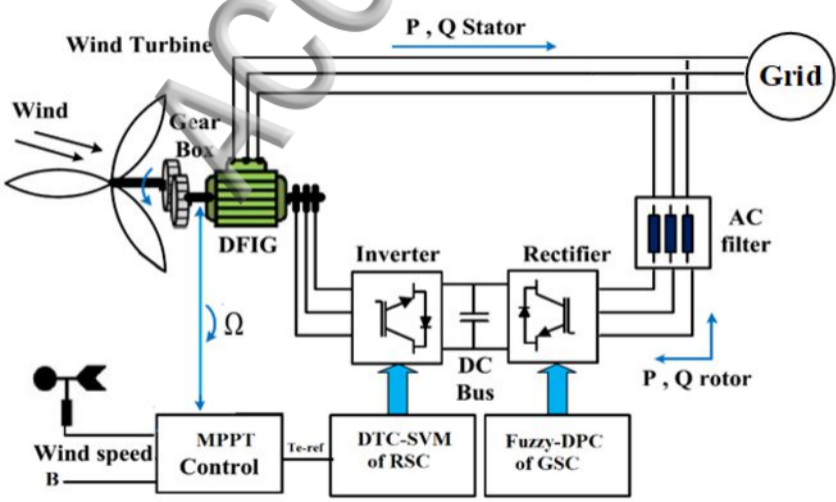
Fig.21: Overall model of SVPWM

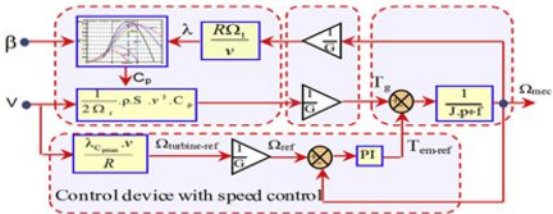
8. Reference

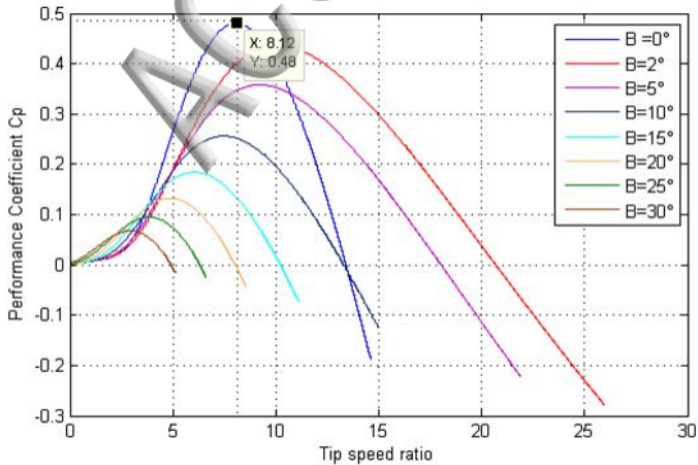
- ¹ B. Vaikundaselvan and M. Kannan, Int. J. Adv. Eng. Technol. **7**, 841 (2016).
- ² K. Selman, B. Seifeddine, M. Youcef, and B. El Madjid, in Ninth IEEE. Int. Conf. On. Ecol. Veh. Renew. Energ.1 (2014).
- ³ N. Amiri, S.M. Madani, T.A. Lipo, and H.A. Zarchi, IEEE Trans. Energy Convers. **27**, 873 (2012).
- ⁴ J. Hu, H. Nian, B. Hu, Y. He, and Z.Q. Zhu, IEEE Trans. Energy Convers. **25**, 1028 (2010).
- ⁵ R. Pena, J.C. Clare, and G.M. Asher, IEE Proc.-Electr. Power Appl. **143**, 231 (1996).
- ⁶ A. Mehdi, A. Reama, H.E. Medouce, S.E. Rezgui, and H. Benalla, in IEEE Int. Symp. On. Power Electron. Electr. Drives Autom. Motion.1128 (2014).
- ⁷ K. Arvind and kumar Brijesh, Int. J. Latest Res. Sci. Technol. **5**, 11 (2016).
- ⁸ I. Takahashi and T. Noguchi, IEEE Trans. Ind. Appl. **820** (1986).
- ⁹ M. Depenbrock, IEEE Trans. Power Electron. **3**, 420 (1988).
- ¹⁰ T. Noguchi, H. Tomiki, S. Kondo, and I. Takahashi, IEEE Trans. Ind. Appl. **34**, 473 (1998).
- ¹¹ Y. Djeriri, A. Meroufel, and A. Massoum, Rev. Roum. Sci. Techn. **54**, 1, (2009).
- ¹² A. Zemmit, S. Messalti, and A. Harrag, Ain Shams Eng. J. (2017).

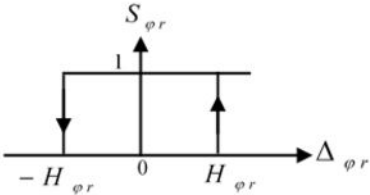
- 13 A. Hassan, A. El-Sawy, and O. Kamel, *J. Eng. Sci. Assiut Univ.* **41**, 199 (2013).
- 14 T. Ghennam, O. Bouhali, D. Maizi, E.M. Berkouk, and B. Francois, in *XXth Int. Conf. On Electr. Mach.* 2178 (2012).
- 15 S. Kouadria, S. Belfedhal, E.-M. Berkouk, and Y. Meslem, in *8th Int. Conf. On Exhib Ecol. Veh. Renew. Energ. I* (2013).
- 16 W. Li, D. Xu, W. Zhang, and H. Ma, in *2nd IEEE Conf. On Ind. Electron. Appl.* 2589 (2007).
- 17 S. Kumsup and C. Tarasantisuk, in *IEEE Int Energy Conf. Exhib. Energy Con.* 7 (2010).
- 18 H. Wu and M. Ding, in *Third Int. Conf. On Electr. Util. Deregul. Restruct. Power Technol.* 2498 (2008).
- 19 R.I. Ovando, J. Aguayo, and M. Cotorogea, in *IEEE Power Electron. Spec. Conf.* 859 (2007).
- 20 L. Lu, Z. Xie, X. Zhang, S. Yang, and R. Cao, in *Second Int. Conf. On Intell. Syst. Des. Eng. Appl.* 967 (2012).
- 21 A. Rolan, A. Luna, G. Vazquez, D. Aguilar, and G. Azevedo, in *IEEE Int. Symp. On Ind. Electron.* 734 (2009).
- 22 A. Boukhelifa and A. Mesri, *Int. J. Multiphysics* **7**, 101 (2013).
- 23 T. Pan, Z. Ji, and Z. Jiang, in *IEEE Energy 2030 Conf. 2008 ENERGY.* 1 (2008).
- 24 O. Barambones, P. Alkorta, and M. De La Sen, in *IEEE Int. Symp. On Ind. Electron.* 364 (2010).
- 25 L. Leclercq, *Univ. Lille Fr.* (2004).
- 26 A. Davigny, *Univ. Libre de Bruxelles*, (2008).
- 27 S. Belfedhal, E.-M. Berkouk, Y. Meslem, and Y. Soufi, *Int. J. Renew. Energy Res.* **2**, 528 (2012).
- 28 S. Kouadria, Y. Messlem, and E.M. Berkouk, in *3rd IEEE Int Renew. Sustain. Energy Conf. I* (, 2015).
- 29 I. Hamzaoui, F. Bouchafaa, and A. Talha, *Int. J. Hydrog. Energy* **41**, 20832 (2016).
- 30 S. Belfedhal and E.L. Berkouk, *Int. J. Renew. Energy Res.* **1**, 152 (2011).
- 31 T. Ghennam, E.M. Berkouk, and B. Francois, in *Int. Conf. On Power Eng. Energy Electr. Drives.* 507(2009).
- 32 H.M. Boulouiha, A. Allali, M. Laouer, A. Tahri, M. Denai, and A. Draou, *Renew. Energy* **80**, 140 (2015).
- 33 Z.A. Alnasir and A.H. Almarhoon, *Int. J. Eng. Technol. IJET* **4**, (2012).
- 34 M.T. Lazim, Al-khishali Muthanna JM, and A.I. Al-Shawi, *Procedia Comput. Sci.* **5**, 505 (2011).
- 35 A.H. Adel, A. Refky, S. Abo-Zaid, and M. Elwany, *J Multidiscip Eng Sci Technol* **1**, 238 (2014).
- 36 A.H. Adel, S. Abo-Zaid, and A. Refky, *J. Multidiscip. Eng. Sci. Technol. JMEST* **2**, 2913 (2015).
- 37 F. Boumaraf, M.L. Bendaas, R. Abdessemed, and S. Belkacem, *Int. J. Electr. Eng. Inform.* **7**, 541 (2015).
- 38 N. Kumar and J. Singh, *Int J. Res. Appl. Sci. Eng. Technol.* **1**, 16 (2013).
- 39 T.G. Habetler, F. Profumo, and M. Pastorelli, in *IEEE Conf. Rec Ind. Appl. Soc. Annu. Meet.* 600 (1992).
- 40 Y.S.K. Babu and G.T.R. Das, *ARPN J. Eng. Appl. Sci.* **5**, 68 (2010).
- 41 H.F. Rashag, S.P. Koh, A.N. Abdalla, N.M. Tan, and K.H. Chong, *J. Power Electron.* **13**, 369 (2013).
- 42 F. Zidani and R.N. Said, *J. Electr. Eng.-Bratisl.* - **56**, 183 (2005).
- 43 D. Rekioua, *Green Energy Technol. Lond. Springer* (2014).
- 44 A.B. Amar, *Int. J. Energ.* **2**, 11 (2017).
- 45 S. Arnalte, J.C. Burgos, and J.L. Rodriguez-Amenedo, *Electr. Power Compon. Syst.* **30**, 199 (2002).
- 46 A. Bakouri, A. Abbou, H. Mahmoudi, and K. Elyalaoui, in *Int Renew. Sustain. Energy Conf.* 334(2014).
- 47 S.A. Gomez and J.L.R. Amenedo, in *IEEE IECON 02 28th Annu. Conf. Of Ind. Electron. Soc.* 3338(2002).
- 48 V.M. Gopala and Y.P. Obulesh, *Int. J. Power Electron. Drive Syst.* **2**, 409 (2012).
- 49 M. Abdelhafidh, M.O. Mahmoudi, L. Nezi, and O. Bouchida, *Int. J. Renew. Energy Res. IJRER* **2**, 300 (2012).
- 50 G.V. Madhav and Y.P. Obulesh, in *IEEE Int. Conf. On Adv. Power Convers. Energy Technol.* 1(2012).
- 51 S. Tamalouzt, T. Rekioua, R. Abdessamed, and K. Idjdarene, in *Proc. Int. Renew. Energy Congr.* 1 (2012).
- 52 S.L. Kaila and H.B. Jani, in *Proc Nat Conf Recent Trends Eng. Technol. VV Nagar Gujarat India BVM Eng. Coll.* (2011).
- 53 S. Tamalouzt, T. Rekioua, and R. Abdessemed, in *IEEE Int. Conf. On Electr. Sci. Technol. Maghreb.* 1(2014).
- 54 G. Buja, D. Casadei, and G. Serra, in *IEEE Int. Symp. On Ind. Electron.* 2 (1997).
- 55 C. Vignesh, S.S. Sheela, E.C.M. Devi, and R. Balachandar, *Int. Refereed J. Eng. Sci.* **3**, 56 (2014).
- 56 M. Uddin and M. Hafeez, *IEEE Trans. Ind. Appl.* **48**, 823 (2012).
- 57 A. Jidin, N.R.N. Idris, A.H.M. Yatim, T. Sutikno, and M.E. Elbuluk, *J. Power Electron.* **11**, 148 (2011).
- 58 D. Casadei, G. Serra, A. Tani, and L. Zarri, *Bull. Pol. Acad. Sci. Tech. Sci.* **54**, (2006).
- 59 D. Casadei, G. Serra, and A. Tani, *IEEE Trans. Ind. Electron.* **48**, 1057 (2001).
- 60 V. Cascone, L. Mantica, and M. Oberti, in *Proc 5rd Eur. Conf Power Electron. Appl. Firenze.* 135 (1989).
- 61 S. Kouro, R. Bernal, H. Miranda, C.A. Silva, and J. Rodríguez, *IEEE Trans. Power Electron.* **22**, 2116 (2007).
- 62 J.-K. Kang and S.-K. Sul, in *IEEE Ind. Appl. Conf. 1998 Thirty-Third IAS Annu. Meet.* 438 (1998).
- 63 P. Gajewski and K. Pieńkowski, *Tech. Trans. Electr. Eng.* 173 (2016).
- 64 D. Casadei, G. Serra, and K. Tani, *IEEE Trans. Power Electron.* **15**, 769 (2000).
- 65 H.W. Van Der Broeck, H.-C. Skudelny, and G.V. Stanke, *IEEE Trans. Ind. Appl.* **24**, 142 (1988).
- 66 T. Sutikno, W.J. Hwa, A. Jidin, and N.R.N. Idris, *Electr. Power Compon. Syst.* **38**, 1546 (2010).
- 67 K.V. Kumar, P.A. Michael, J.P. John, and S.S. Kumar, *ARPN J. Eng. Appl. Sci.* **5**, 61 (2010).
- 68 N.A. Salim, M.A. Kaprowi, and A.A. Abd Samat, *Pertanika J. Sci. Technol.* **25**, 171 (2017).
- 69 S. Manivannan, K. Senthilnathan, P. Selvabharathi, and K. Rajalashmi, *Int. J. Emerg. Eng. Res. Technol.* **2**, 1 (2014).
- 70 A. Gupta, H. Gupta, and A.K. Tiwari, *Natl. POWER Syst. Conf.* 833 (2002).
- 71 M. Zelechowski, *Rozpr. Doktorska Warszawa* (2005).
- 72 V. Kumar and S. Rao, *Leonardo J. Sci.* **10**, 27 (2011).
- 73 S. Allirani and V. Jagannathan, *Int. J. Comput. Sci.* **7**, (2010).
- 74 A.A. Nafeh and M.M.A. Salama, *J. Electr. Eng.* 1 (2010).
- 75 J.M.R. Malla, M.K. Sahu, and P.K. Subudhi, in *IEEE Int. Conf. on Electr. Electron. Optim. Tech.* 4941 (2016).
- 76 A. Manuel and J. Francis, *Int. J. Adv. Res. Electr. Electron. Instrum. Eng.* **2**, (2013).
- 77 K. Chikh, A. Saad, M. Khafallah, D. Yousfi, F.Z. Tahiri, and M. Hasoun, *Int. J. Power Electron. Drive Syst.* **8**, (2017).
- 78 N. Taghizadegan, M.B. Sharifian, A. Daghigh, and E. Babaei, in *IEEE Int. Conf. On Electr. Mach. Syst.* 1 (2011).
- 79 S.V. Paturca, M. Covrig, and L. Melcescu, in *Proc. 6th Int. Conf. Electr. Power Syst. High Volt. Electr. Mach.* 111 (2006).

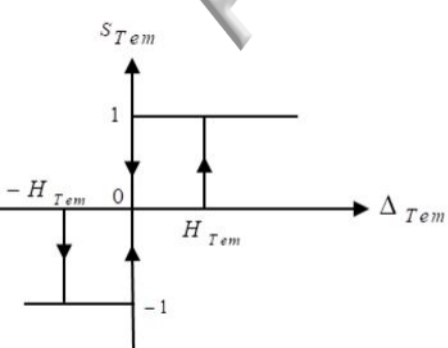
- ⁸⁰ D. Swierczynski, M. Kazmierkowski, and F. Blaabjerg, in Proc IEEE Int Symp Ind Electron.723 (2002).
- ⁸¹ H.F. Rashag, N.M. Tan, S.P. Koh, A.N. Abdalla, K.H. Chong, and S.K. Tiong, Res. J. Appl. Sci. Eng. Technol. **7**, 875 (2014).
- ⁸² J.-K. Kang and S.-K. Sul, IEEE Trans. Ind. Appl. **35**, 1076 (1999).
- ⁸³ Y. Djeriri, A. Meroufel, A. Massoum, and Z. Boudjema, J. Electr. Eng. **14**, 159 (2014).
- ⁸⁴ G. Abad, M.A. Rodriguez, G. Iwanski, and J. Poza, IEEE Trans. Power Electron. **25**, 442 (2010).
- ⁸⁵ Y. Djeriri, A. Meroufel, A. Massoum, and Z. Boudjema, J. Electr. Eng. JEE Rom. **14**, 196 (2014).
- ⁸⁶ A. Boulahia, K. Nabti, and H. Benalla, Int. J. Electr. Comput. Eng. **2**, 425 (2012).
- ⁸⁷ J.B. Alaya, A. Khedher, and M.F. Mimouni, J. Electr. Eng. LEE **6**, 744 (2011).
- ⁸⁸ A. Boukadoum, T. Bahi, and A. Bouguerne, Proc. Int. Conf. Recent Adv. Electr. Syst. 165 (2016).
- ⁸⁹ M. Malinowski, M. Jasinski, and M.P. Kazmierkowski, IEEE Trans. Ind. Electron. **51**, 447 (2004).
- ⁹⁰ A. Bouafia, J.-P. Gaubert, and F. Krim, IEEE Trans. Power Electron. **25**, 228 (2010).
- ⁹¹ J. Lamterkati, M. Khafallah, L. Ouboubker, and A. Elafia, Int. J. Sci. Res. **4**, 336 (2015).
- ⁹² A. Bouafia, F. Krim, and J.-P. Gaubert, IEEE Trans. Ind. Electron. **56**, 1984 (2009).
- ⁹³ M. Jamma, A. Bennassar, M. Barara, and M. Akherraz, Int. J. Power Electron. Drive Syst. **8**, 979 (2017).
- ⁹⁴ P. Tripura, Y.K. Babu, and Y.R. Tagore, ACEEE Int J Control Syst. Instrum. **2**, 34 (2011).
- ⁹⁵ S. Kushwah, A.K. Wadhvani, and S. Wadhvani, Int. J. Sci. Eng. Technol. **3**, 0592 (2014).
- ⁹⁶ M. Shrivastava, M.V. Singh, and S. Pattnaik, Int. J. Eng. Res. Appl. **2**, 2209 (2012).
- ⁹⁷ B.G. Sujatha and G.S. Anitha, Int. J. Recent Innov. Trends Comput. Commun. **5**, 11 (2016).
- ⁹⁸ P.A. Michael and N. Devarajan, Int. J. Eng. Technol. **1**, 208 (2009).
- ⁹⁹ S. Altay and S. Güngör, (2001).
- ¹⁰⁰ B. Rashidi and M. Sabahi, Int. J. Mod. Educ. Comput. Sci. **5**, 62 (2013).
- ¹⁰¹ G.K. Nisha, S. Ushakumari, and Z.V. Lakapampil, in Proc. Int. Multi Conf. Eng. Comput. Sci. (2012).
- ¹⁰² M. Kubeitari, A. Alhusayn, and M. Alnahar, World Acad. Sci. Eng. Technol. **6**, 644 (2012).
- ¹⁰³ Z.-G. Wang, J.-X. Jin, Y.-G. Guo, and J.-G. Zhu, J. Electron. Sci. Technol. **6**, 191 (2008).
- ¹⁰⁴ B. Wu, H.-P. Converters, and A.C. Drives, N. J. **3** (2006).
- ¹⁰⁵ I. Ahmed and V.B. Borghate, IET Power Electron. **7**, 604 (2013).
- ¹⁰⁶ S. Manivannan, S. Veerakumar, P. Karuppusamy, and A. Nandhakumar, Int. J. Innov. Res. Electr. Electron. Instrum. CONTROL Eng. **2**, 1959 (2014).
- ¹⁰⁷ J. Soltani, G.R.A. Markadeh, N.R. Abjadi, and H.W. Ping, in IEEE Int. Conf. On Electr. Mach. Syst. 497 (2007).
- ¹⁰⁸ A. Chikhi, Majlesi J. Mechatron. Syst. **2**, (2013).
- ¹⁰⁹ S. Belkacem, F. Naceri, and R. Abdessemed, J. Electr. Eng. **10**, 79 (2010).
- ¹¹⁰ M. El Azzaoui and H. Mahmoudi, Int. J. Adv. Comput. Res. **6**, 153 (2016).

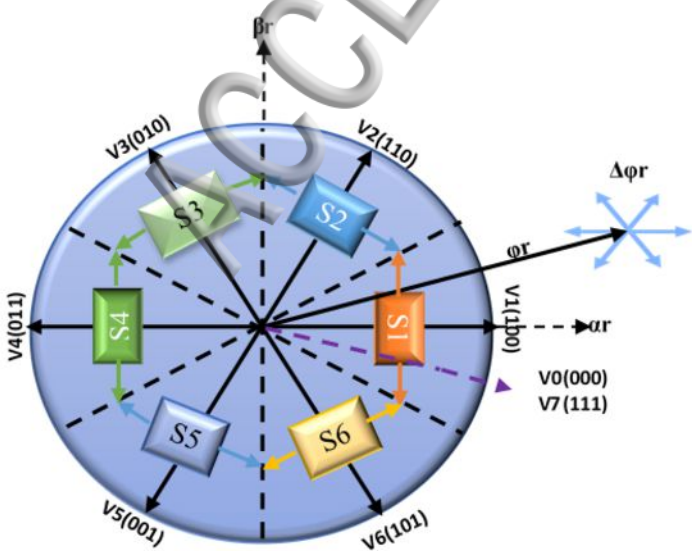


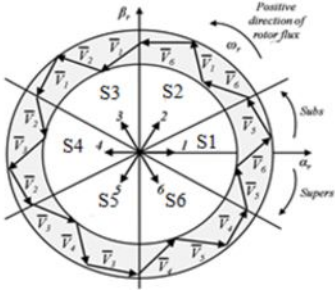


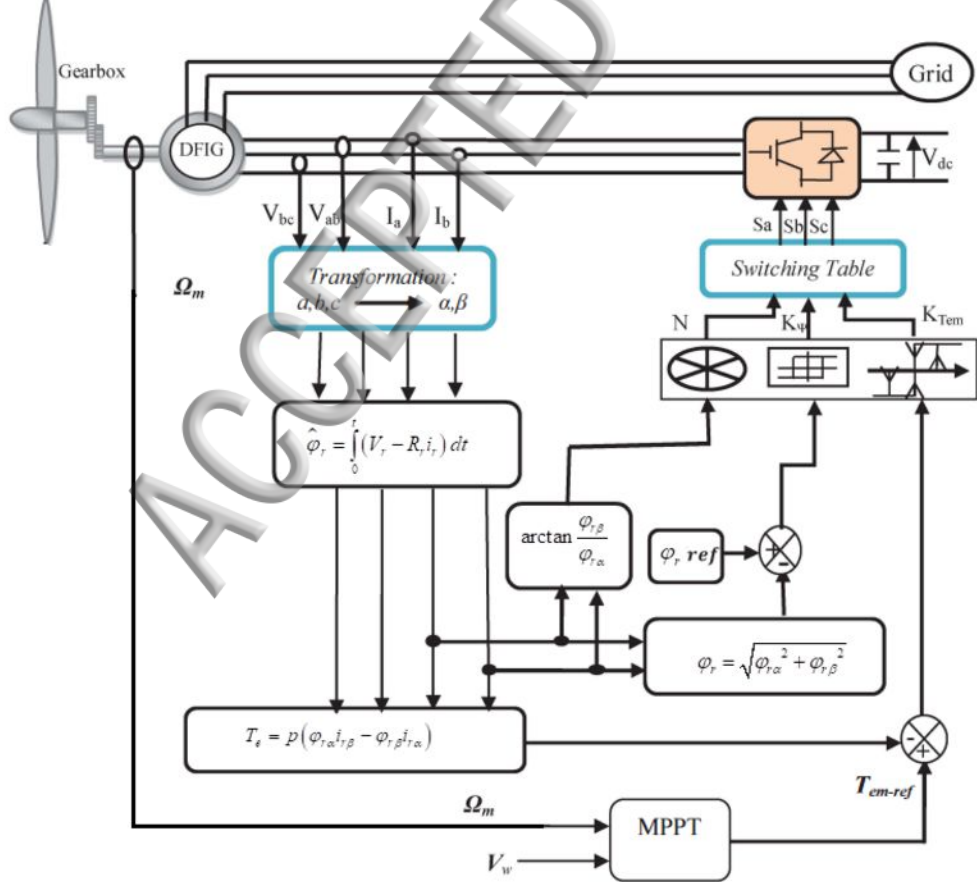


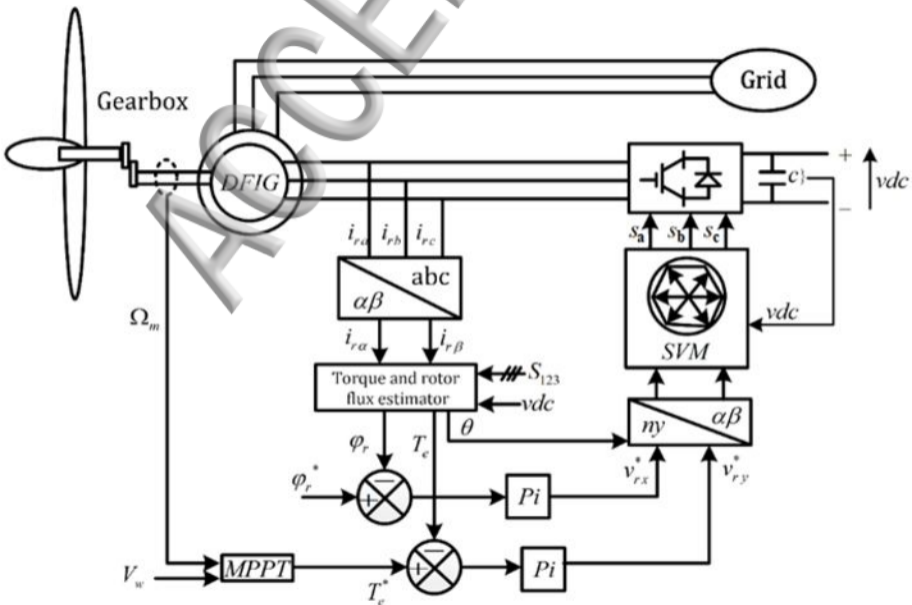


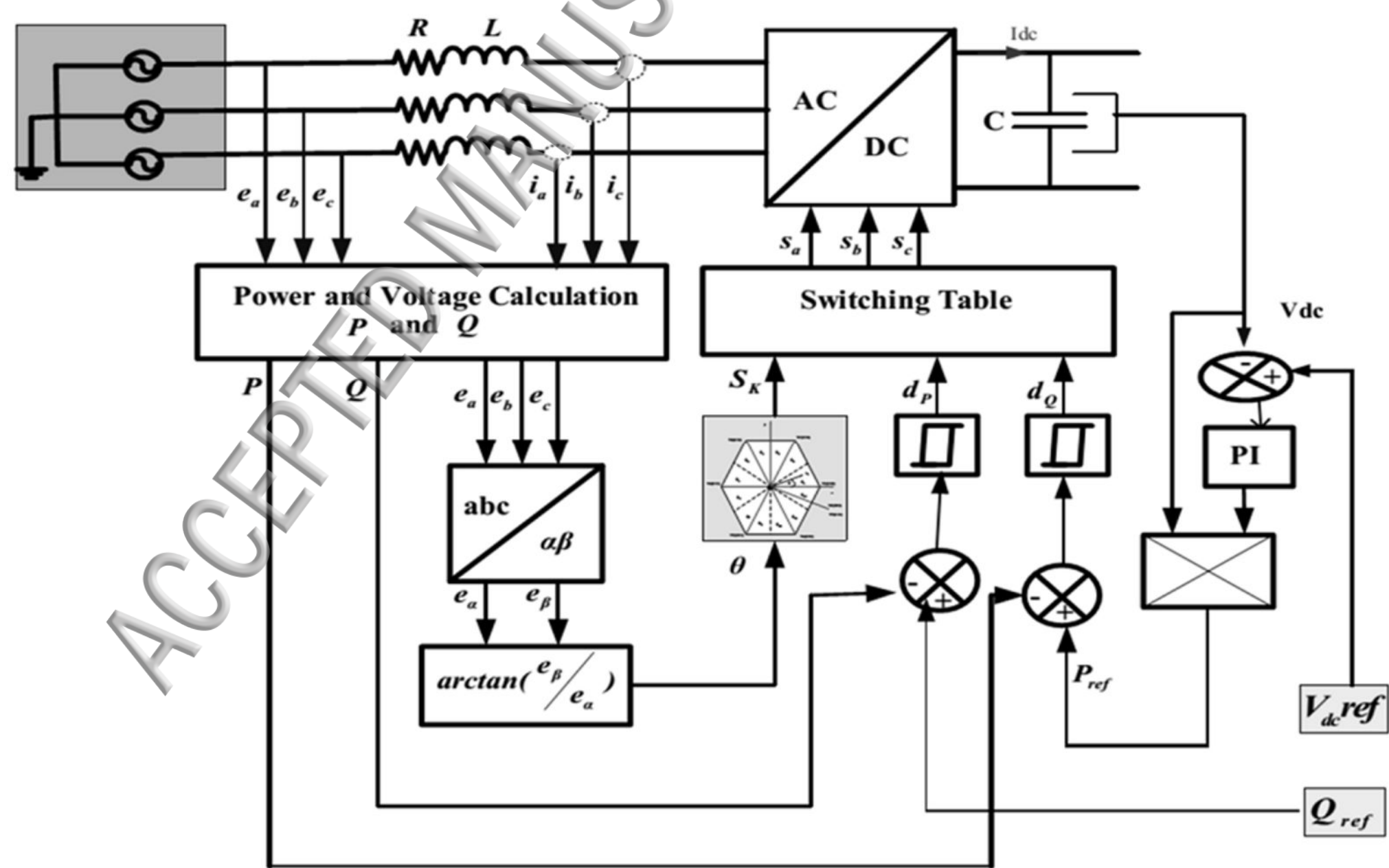


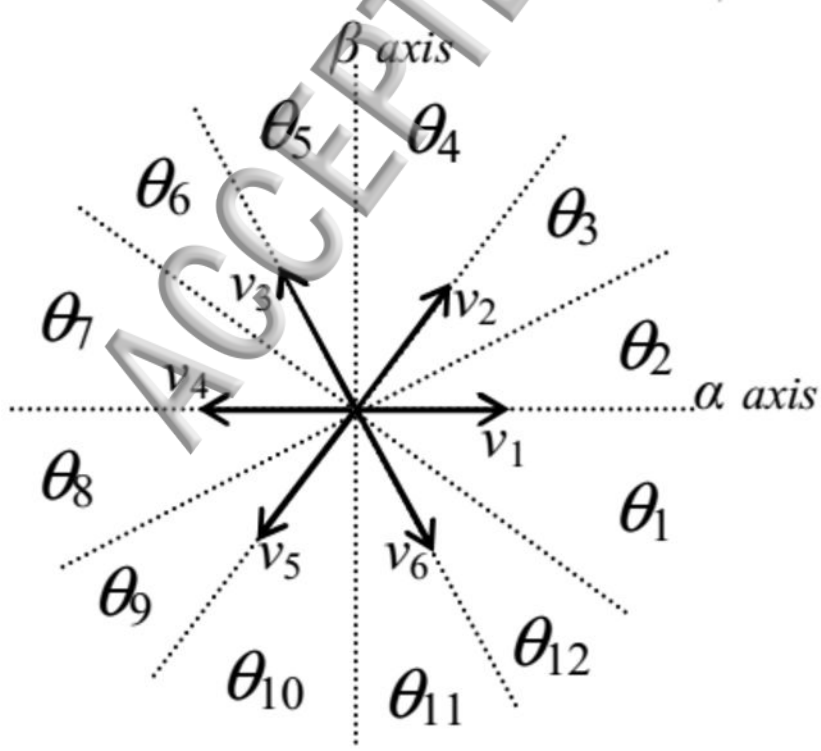


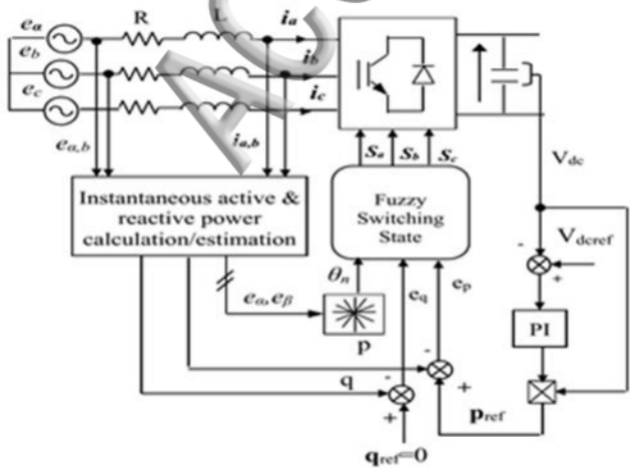




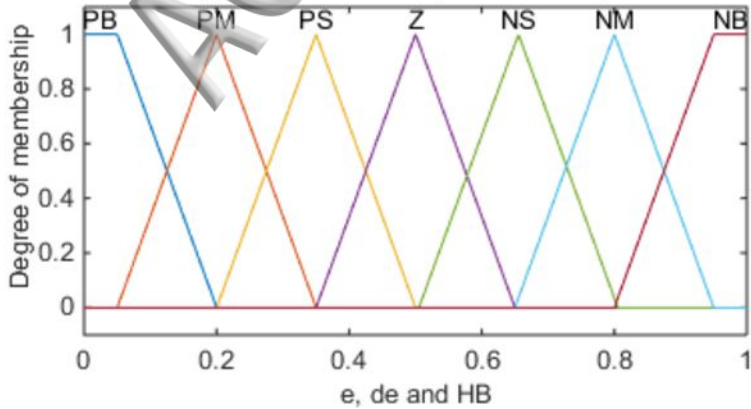


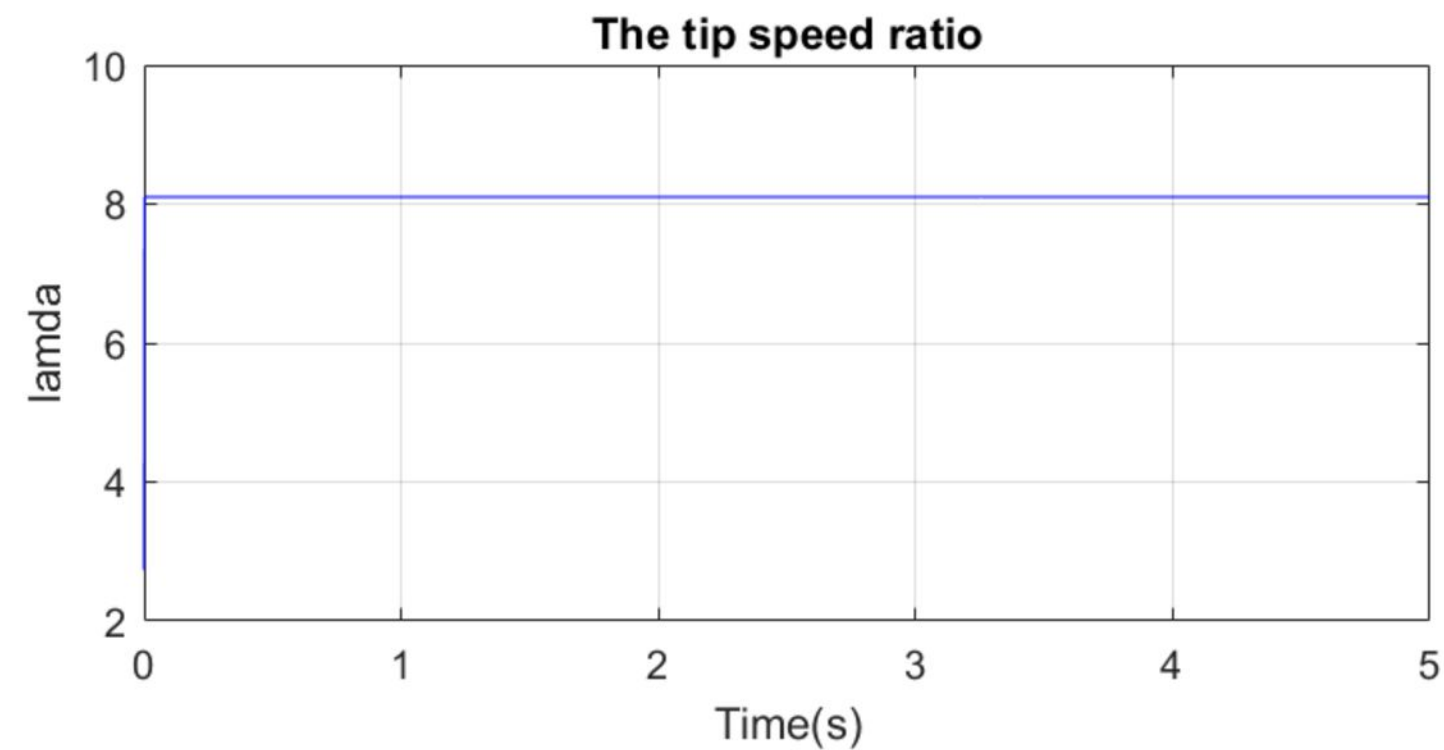
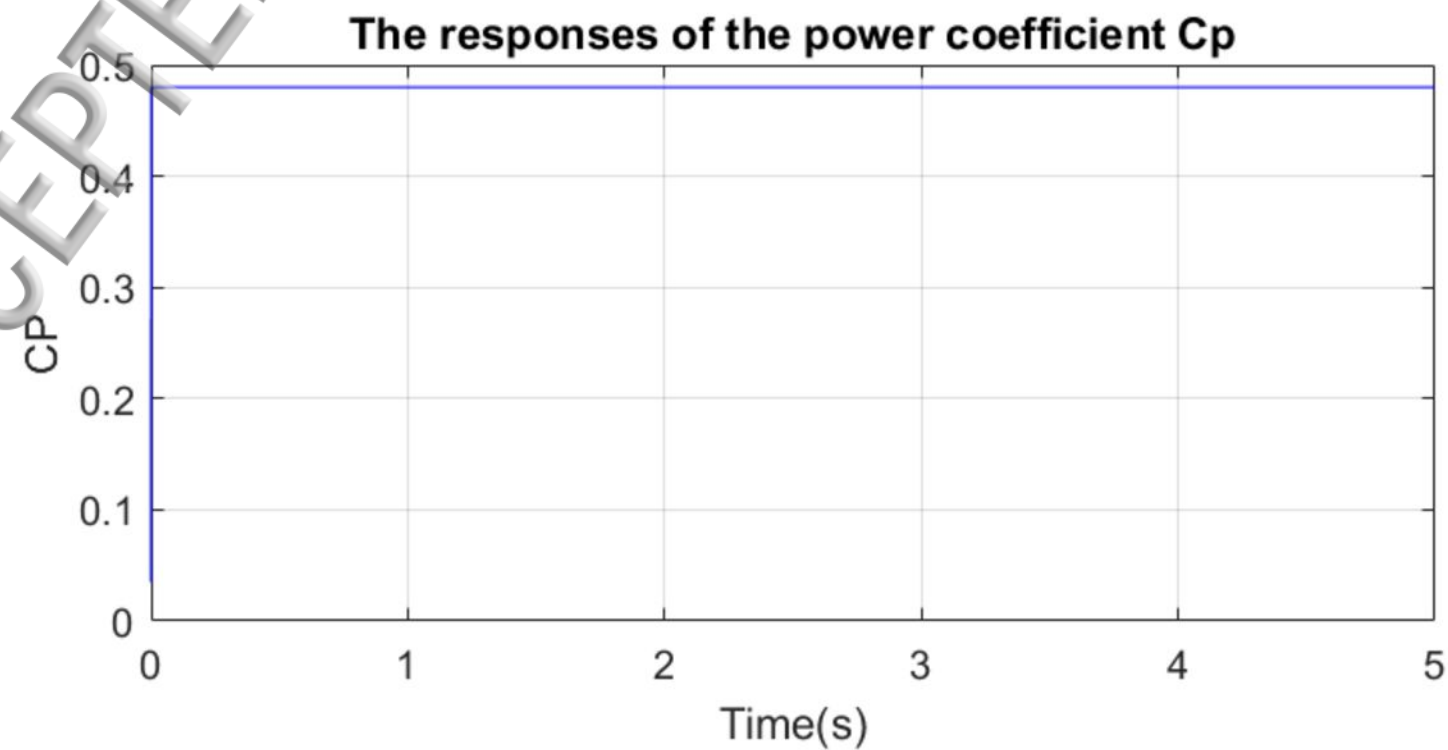
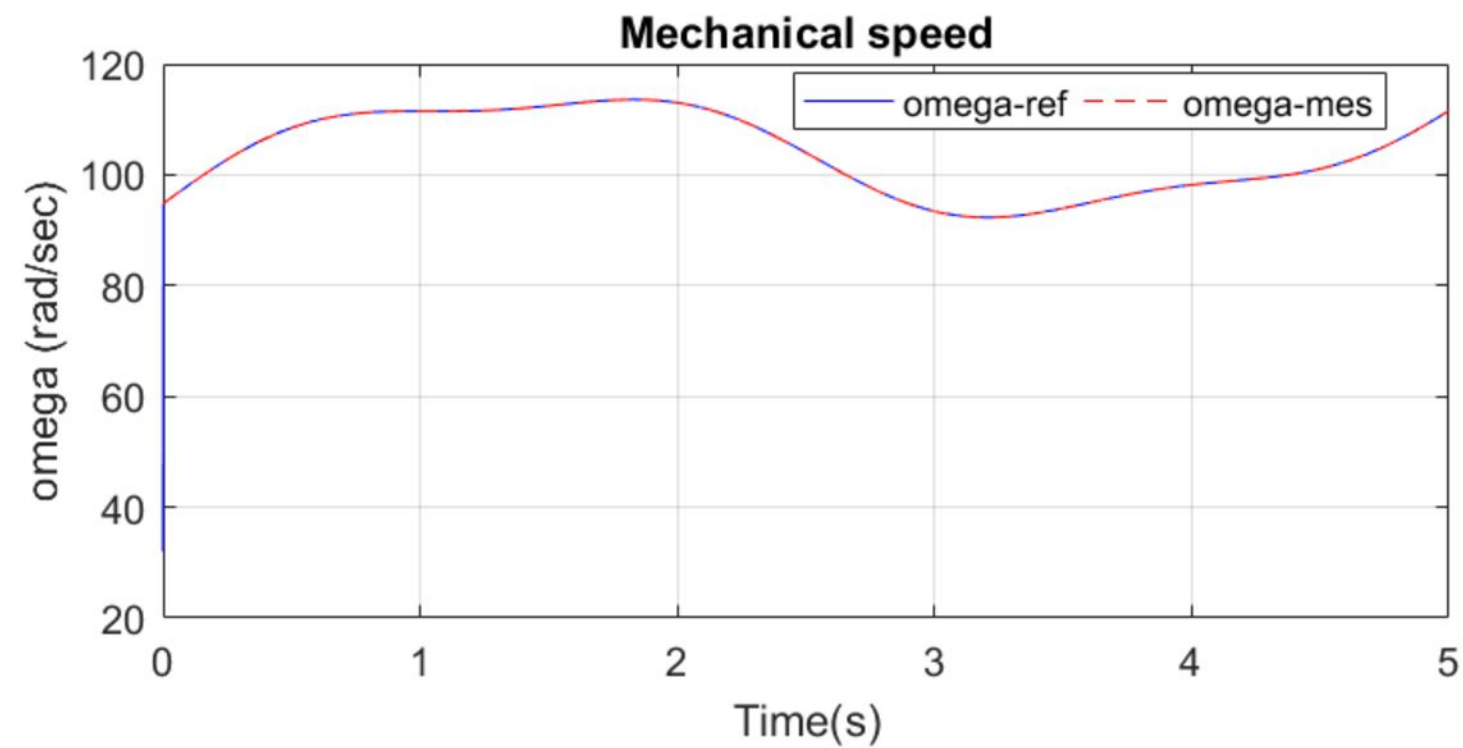
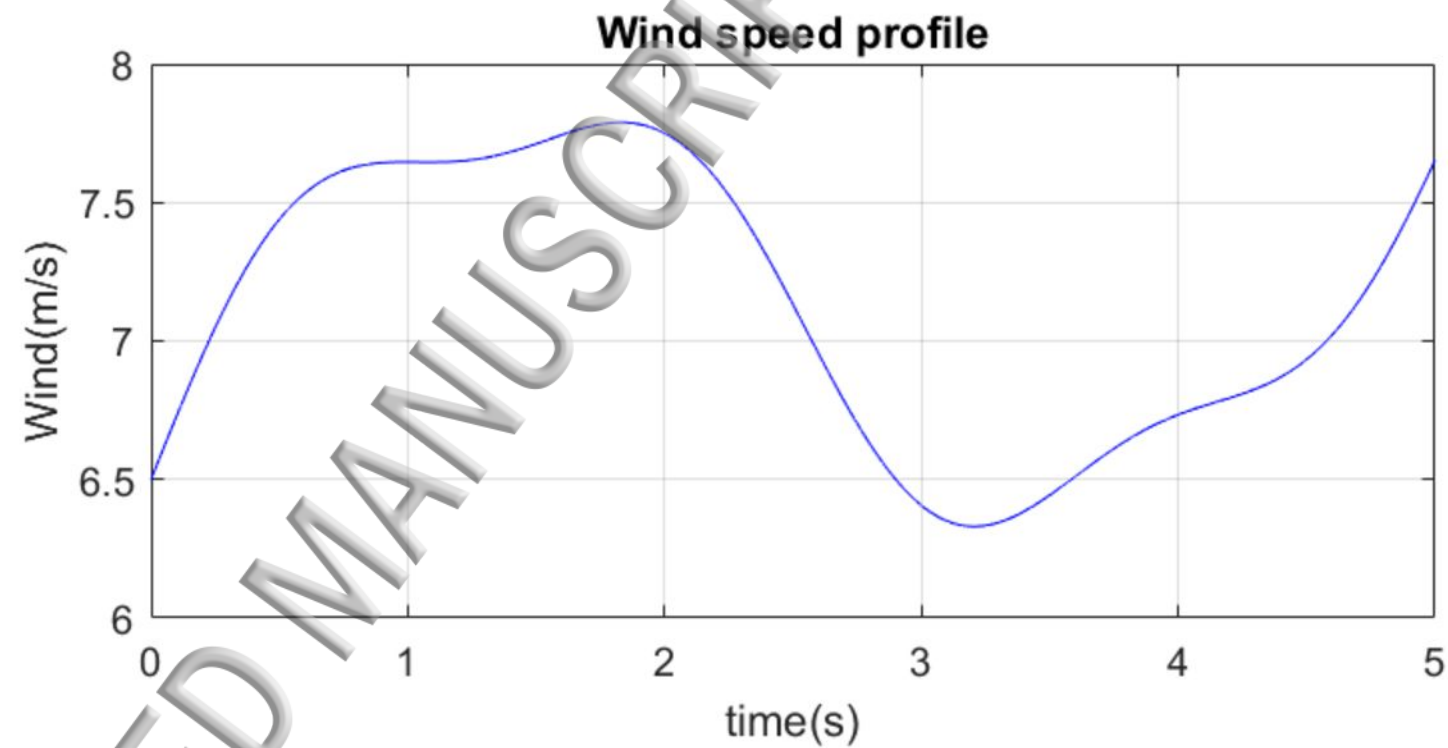


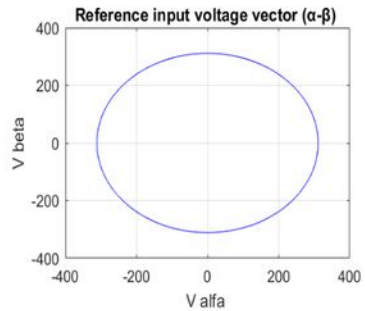
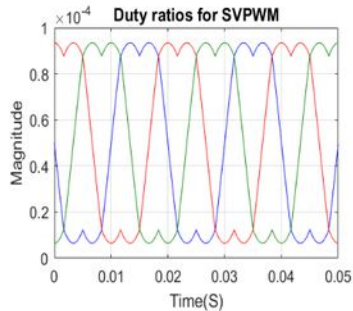
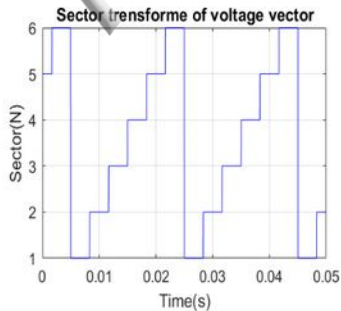
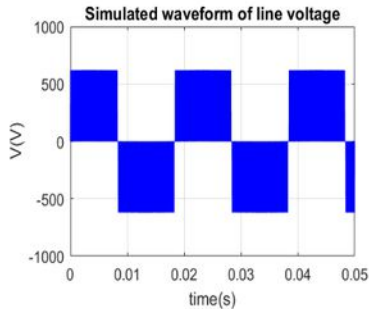
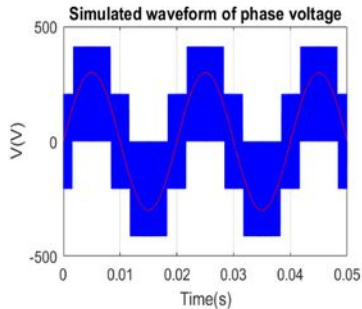
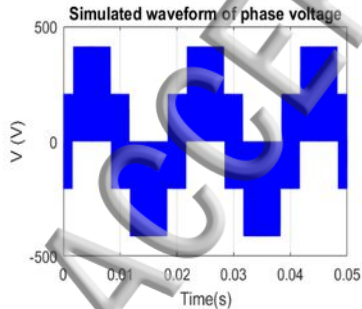


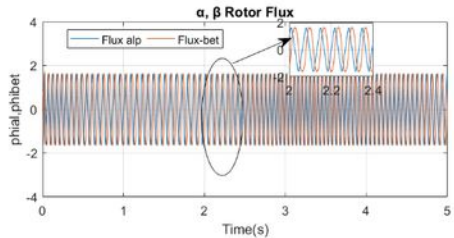
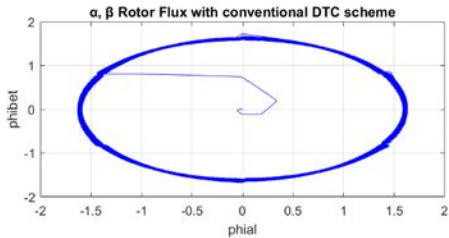
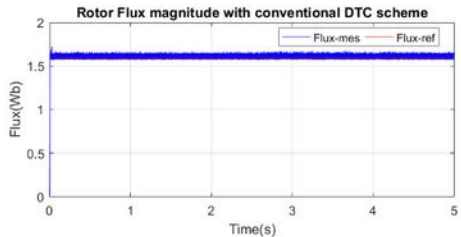
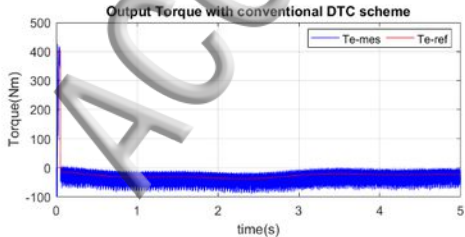


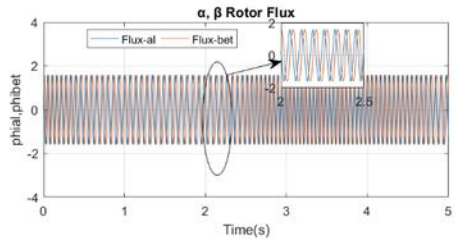
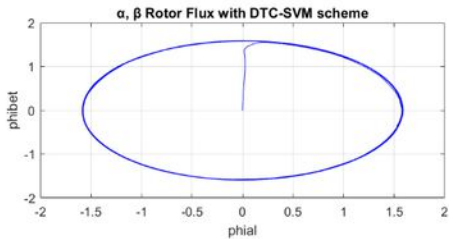
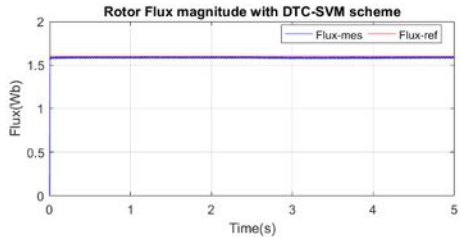
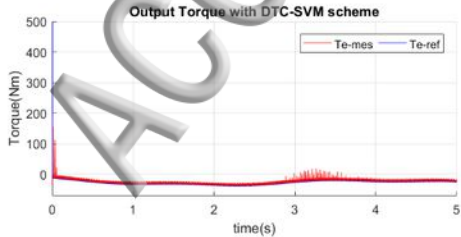
Membership functions of input and output variables



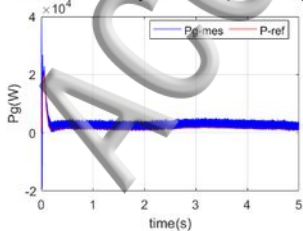




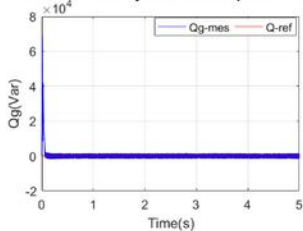




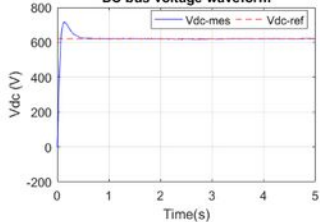
Waveform of the injected active power into grid



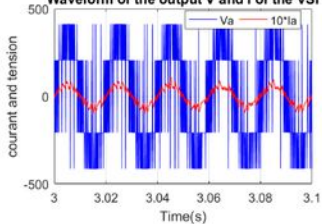
Waveform of the injected reactive power into grid



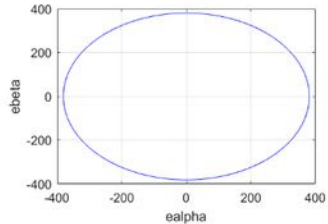
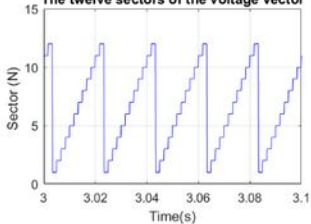
DC bus voltage waveform



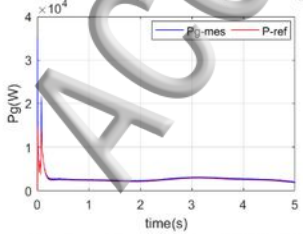
Waveform of the output V and I of the VSI



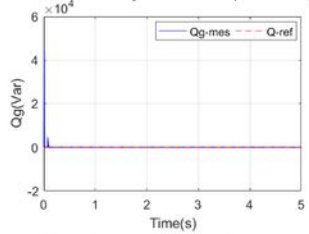
The twelve sectors of the voltage vector



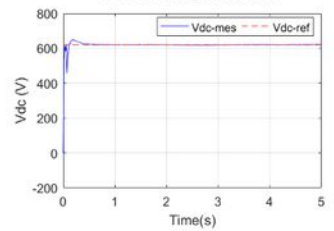
Waveform of the injected active power into grid



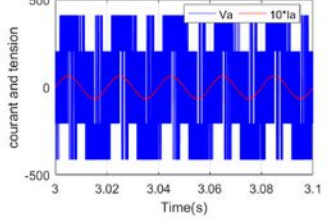
Waveform of the injected reactive power into grid



DC bus voltage waveform



Waveform of the output V and I of the VSI



The twelve sectors of the voltage vector

